

CHARACTERIZATION OF THE EVOLUTION OF 2219-T87 ALUMINUM AS A  
FUNCTION OF THE SELF-REACTING FRICTION STIR WELDING PROCESS

by

KATHRYN V. ANDERSON

S.R. DANIEWICZ, COMMITTEE CHAIR  
ROBERT AMARO, COMMITTEE CO-CHAIR  
PETE MCKEIGHAN  
MARK WEAVER

A THESIS

Submitted in partial fulfillment of the requirements  
for the degree of Master of Science in the  
Department of Mechanical Engineering  
in the Graduate School of  
The University of Alabama

TUSCALOOSA, ALABAMA

2019

Copyright Kathryn V. Anderson 2019  
ALL RIGHTS RESERVED

## ABSTRACT

The self-reacting friction stir welding (SR-FSW) process is a primary method used by NASA to construct the Space Launch System (SLS) vehicle. This method uses large scale shear to plastically deform and mechanically mix base materials. This solid-state process causes the fabricated material to reach a temperature below the melting point, and as such, there are lower residual stresses and less warping than that observed in traditional fusion welding processes. The process parameters responsible for heat generation in the SR-FSW process include: the tool rotational speed, the tool translational speed, the crown plunge force, and the root/pin reaction force. Optimization of these process parameters is required to produce sound welded joints with the appropriate microstructural constituents.

This work characterizes the effect of SR-FSW on AA2219-T87. Specifically, the material's microhardness, strength, and  $\theta$ -phase evolution are studied as a function of time and temperature. These data sets are compared to the microhardness in the friction stir weld stir zone, thermo-mechanically affected zone (TMAZ), heat affected zone (HAZ), and base material. Additionally, residual stresses produced as a function of the friction stir welding process are quantified. Furthermore, fatigue crack growth rate data and plane-strain fracture toughness data of the welded material are compared to that of the base material. Finally, all data collected is used to calibrate a tool that determines the relative contribution from various strengthening mechanisms to the overall strength of the weld.

## ACKNOWLEDGEMENTS

First and foremost, I would like to thank my soon-to-be husband, Kevin, for his patience and support over the last two years. I would not be where I am today without his encouragement.

I would also like to acknowledge and thank my co-advisors, Dr. Steve Daniewicz and Dr. Robert Amaro. I would not be here without Dr. Daniewicz's convincing to give graduate school a try. I have benefited immensely from the time he has spent mentoring me, both on campus and on the tennis court. Likewise, I am greatly appreciative of the work that Dr. Robert Amaro has done in teaching me how to be a better engineer and scientist. I cannot thank both of them enough for shaping my future in the way that they have.

I would further like to acknowledge the remaining members of my advisory committee, Dr. Pete McKeighan and Dr. Mark Weaver, for their willingness to support my research.

I would also like to thank my fellow researchers who I have worked with during my time at The University of Alabama: Cole Cauthen, Emma Burford, and George Stubblefield.

I would also like to acknowledge Jeff Sowards at NASA Marshall Space Flight Center in Huntsville, Alabama, for his support of this project.

Last, but most certainly not least, I would like to thank my father and mother, John and Stephanie Anderson. I would not be who I am today without your teaching, love, and support.

## CONTENTS

ABSTRACT.....	ii
ACKNOWLEDGEMENTS .....	iii
LIST OF TABLES.....	vii
LIST OF FIGURES .....	viii
CHAPTER 1 INTRODUCTION .....	1
1.1 Research Motivation .....	1
1.2 Research Objectives .....	1
1.3 Overview of Thesis .....	2
CHAPTER 2 LITERATURE REVIEW .....	3
2.1 Introduction.....	3
2.2 Description of AA2219-T87 .....	4
2.3 Precipitate Strengthening .....	4
2.4 Self-Reacting Friction Stir Welding .....	7
2.5 Strengthening Mechanisms Manifesting in Crystalline Solids .....	9
2.5.1   Measurement of Strength .....	10
2.5.2   Solid Solution Strengthening .....	11
2.5.3   Grain Size Strengthening .....	11
2.5.4   Grain Orientation Strengthening .....	12
2.5.5   Precipitate Strengthening .....	13
2.6 Fatigue Crack Growth Testing.....	14

2.7 Fracture Toughness Testing .....	20
<b>CHAPTER 3 VIRGIN MATERIAL CHARACTERIZATION .....</b>	<b>23</b>
3.1 Introduction.....	23
3.2 Material Selection .....	23
3.3 Property Diagram.....	24
3.4 Phase Transformation Kinetics .....	25
3.5 Grain Size.....	29
<b>CHAPTER 4 SELF-REACTING FRICTION STIR WELD CHARACTERIZATION .....</b>	<b>32</b>
4.1. Introduction.....	32
4.2. Welded Material Characterization .....	33
4.2.1. Residual Stresses.....	33
4.2.2. Grain Morphology.....	37
4.2.3. Microhardness .....	39
4.3. Fatigue Crack Growth and $K_{IC}$ Testing.....	40
4.3.1. Specimens.....	41
4.3.2. FCG Test Matrices .....	42
4.3.3. FCG Test Results and Conclusions.....	43
4.3.4. $K_{IC}$ Test Results and Conclusions .....	45
4.4. Model Implementation.....	47
<b>CHAPTER 5 CONCLUSIONS AND FUTURE WORK .....</b>	<b>53</b>
5.1. Conclusions.....	53
5.2. Future Work .....	53

REFERENCES .....	55
APPENDIX.....	57

## LIST OF TABLES

Table 2.1. <i>AA2219-T87 nominal chemical composition</i> (Bauccio, 1993). ....	4
Table 3.1. <i>Tensile properties for AA2219</i> (ASM, n.d.).....	23
Table 3.2. <i>Expected microstructure and relative strength measurement of three thermal histories</i> .....	29
Table 3.3. <i>Measured grain size for the virgin AA2219-T87</i> . ....	30
Table 3.4. <i>Measured grain size along the longitudinal direction of the short plane for the heat treated AA2219. Data collected after 2.8 hours of exposure</i> .....	31
Table 4.1. <i>Grain size measurements on the longitudinal plane for AA2219 aluminum SR-FSW by use of nominal process parameters. All units are in microns.</i> .....	38
Table 4.2. <i>Load amplitudes used for FCG tests</i> .....	40
Table 4.3. <i>Average crack opening load as a function of weld location and <math>\Delta K</math></i> .....	44
Table 4.4. <i><math>K_{IC}</math> values for locations of SR-FSW. * indicates invalid test per ASTM E399</i> .....	46
Table 4.5. <i>Predicted precipitate strengthening contributions for stir zone and TMAZ for five process parameter sets</i> .....	52

## LIST OF FIGURES

<i>Figure 2.1.</i> Example of particle shearing (a) and Orowan looping (b) (Ashby, 2009; Dieter, 1986). ....	5
<i>Figure 2.2.</i> The relationship between aging and yield strength for an Al-4 wt% Cu alloy (Ashby, 2009). Note the cutting stress and bowing stress lines.....	6
<i>Figure 2.3.</i> Calorimetric data found in literature (Papazian, 1982). ....	7
<i>Figure 2.4.</i> Schematic of a generic SR-FSW tool and the tool-material interaction (Bjorkman, 2003). ....	8
<i>Figure 2.5.</i> Relationship between microhardness and UTS for AA2219 (Raza, 2011). ....	10
<i>Figure 2.6.</i> Loading modes for a crack (Stephens, 2001). ....	14
<i>Figure 2.7.</i> Schematic of fatigue crack growth behavior and corresponding regions of crack growth (Stephens, 2001). ....	16
<i>Figure 2.8.</i> Illustration the crack faces during (a) PICC and (b) RICC (Anderson, 2005). ....	18
<i>Figure 2.9.</i> Standard dimensions of C(T) sample per ASTM E647. Dimensions in millimeters (inches). ....	19
<i>Figure 2.10.</i> Method of determining $P_Q$ from load and displacement data from a $K_{IC}$ Test (ASTM E647). ....	22
<i>Figure 3.1.</i> Property diagram of AA2219-T87 generated for maximum allowable chemical composition of all alloying elements. ....	25
<i>Figure 3.2.</i> Non-stressed isothermal microhardness results collected after 2.8 hours of thermal exposure compared to calorimetric data from Papazian. ....	27
<i>Figure 3.3.</i> Non-stressed isothermal data for multiple thermal histories and the expected microstructures.....	28
<i>Figure 3.4.</i> Schematic of Longitudinal (L), Transverse (T), and Short (S) directions. The orientation of each plane is defined by the direction normal to the plane of interest. ....	30

<i>Figure 3.5.</i> Electron backscatter detector grain orientation map with respect to the short orientation .....	31
<i>Figure 4.1.</i> Schematic indicating locations of residual stress spot measurements. ....	34
<i>Figure 4.2.</i> Residual stress values in the longitudinal direction measured at spot locations indicated in Figure 4.1 (crown side of plate). Magnitudes are MPa.....	35
<i>Figure 4.3.</i> Residual stress values in the transverse direction measured at spot locations indicated in Figure 4.1 (crown side of plate). Magnitudes are MPa.....	36
<i>Figure 4.4.</i> Line scan of longitudinal residual stresses.....	37
<i>Figure 4.5.</i> Micrographs of grain size in respective locations of SR-FSW.....	38
<i>Figure 4.6.</i> Microhardness map of AA2219-T87 SR-FSW built using the optimum process parameter set. ....	40
<i>Figure 4.7.</i> Final FCG and $K_{IC}$ sample geometry. All units are in millimeters. Thickness $B$ is 12.7 millimeters. ....	41
<i>Figure 4.8.</i> Images of C(T) specimens showing where the stir zone (blue) and TMAZ (yellow) exist relative to the crack (red) intended path. Image (a) and image (b) represent stir zone and TMAZ samples, respectively.....	42
<i>Figure 4.9.</i> Fatigue crack growth data for base material, TMAZ, and stir zone samples. ....	43
<i>Figure 4.11.</i> Process parameter sets to be studied circled in purple. The optimum set is indicated by the green cross. ....	49
<i>Figure 4.12.</i> Process parameter set #1. Nominal traversing speed, low rotational speed .....	50
<i>Figure 4.13.</i> Process parameter set #2. Nominal traversing speed, high rotational speed. ....	51
<i>Figure A.1.</i> Micrograph of base material (short orientation) aged at room temperature, 20°C. ....	57
<i>Figure A.2.</i> Micrograph of base material (longitudinal orientation) aged at room temperature, 20°C. ....	57
<i>Figure A.3.</i> Micrograph of base material (transverse orientation) aged at room temperature, 20°C.....	58
<i>Figure A.4.</i> Micrograph of base material aged at room temperature, 150°C.....	59
<i>Figure A.5.</i> Micrograph of base material aged at room temperature, 250°C.....	59

<i>Figure A.6.</i> Micrograph of base material aged at room temperature, 300°C.....	60
<i>Figure A.7.</i> Micrograph of base material aged at room temperature, 425°C.....	60
<i>Figure A.8.</i> Representative FCG and $K_{IC}$ fracture surfaces for the base material (A), stir zone (B), and TMAZ (C). .....	61
<i>Figure A.9.</i> Representative FCG and $K_{IC}$ fracture surfaces for the base material (A), stir zone (B), and TMAZ (C). .....	62
<i>Figure A.10.</i> Representative FCG and $K_{IC}$ fracture surfaces for the base material (A), stir zone (B), and TMAZ (C). .....	62
<i>Figure A.11.</i> Representative load-displacement plot for base material $K_{IC}$ sample. ....	63
<i>Figure A.12.</i> Representative load-displacement plot for stir zone $K_{IC}$ sample. ....	64
<i>Figure A.13.</i> Representative load-displacement plot for TMAZ $K_{IC}$ sample. ....	65
<i>Figure A.14.</i> Model results of process parameter set #3. Low traversing speed, nominal tool rotational rate.....	66
<i>Figure A.15.</i> Model results of process parameter set #4 High traversing speed, nominal tool rotational rate.....	67

## CHAPTER 1 INTRODUCTION

### 1.1 Research Motivation

The aluminum alloy (AA) 2219-T87 is the primary alloy used in the construction of the liquid hydrogen and liquid oxygen tanks of NASA's Space Launch System (SLS) vehicle. AA2219 is aluminum-copper, age hardenable alloy that derives a portion of its strength from Al<sub>2</sub>Cu precipitates, or theta phases. The self-reacting friction stir welding (SR-FSW) process is extensively used for joining AA2219-T87 panels. This process is a solid-state welding technique where a cylindrical pin tool with two disk-like shoulders mechanically stirs the parent material to join two surfaces. The melting point of the material is not reached, and as such, there is less warpage and residual stress when compared with traditional fusion welding processes.

While the temperatures experienced during the SR-FSW proves are below the melting point of the material, they are still high enough to cause dissolution of the strengthening phases within the alloy. Additionally, the residual stresses induced by the process may cause a change in the properties of the welded joint. In order to ensure the reliability of the cryogenic tanks on the SLS vehicle, the structural integrity of the SR-FSW joints must be quantified.

### 1.2 Research Objectives

This research aims to characterize the effect of SR-FSW on AA2219-T87. Specifically, this research provides results and analysis of multiple experiments to characterize microscopic and macroscopic properties of both virgin and SR-FSW AA2219-T87. The experimental data collected and the background from literature provide data to calibrate the development of an

analytical tool that estimates contributions to ultimate tensile strength (UTS) from multiple strengthening mechanisms common in crystalline materials.

### 1.3 Overview of Thesis

This work is formatted such that each chapter may be a stand-alone document, subsequent to minimal modifications. CHAPTER 2 is comprised of a literature review focusing upon the aluminum alloy 2219-T87 and its applications and primary strengthening mechanisms. Other topics include the self-reacting friction stir welding process, the standards associated with the FCG and  $K_{IC}$  testing, and an overview of strengthening mechanisms that effect crystalline metals. CHAPTER 3 provides insight into the choice of material for this work as well as an initial characterization of the material. CHAPTER 4 details the self-reacting friction stir welding process. Specifically, it presents the results of residual stress measurements, grain morphology quantification, phase transformation kinetics, and ultimate tensile strength (UTS) predictions from microhardness measurements. Data from fatigue crack growth (FCG) and plane-strain fracture toughness ( $K_{IC}$ ) experiments are also presented. The calibration and results of a model that quantifies the relative contributions of strengthening mechanism to the ultimate tensile strength of SR-FSW AA2219 is also discussed. Conclusions and recommendations for future work are discussed in CHAPTER 5.

## CHAPTER 2 LITERATURE REVIEW

### 2.1 Introduction

Self-reacting friction stir welding is the method used extensively by NASA to join AA2219-T87 panels in the construction of the Space Launch System vehicle. This method uses large scale shear to plastically deform and mechanically mix base materials. This solid-state process does not reach the melting point of materials, and as such, there is less warpage and residual stress than traditional fusion welding processes. Although the melting temperature of the material is not reached in the SR-FSW process, dissolution of the primary strengthening phases found in age hardenable alloys occurs with heat input. In order to ensure ideal microstructure and properties exist in the weld, the heat input for each process parameter set must be understood.

This work details the data collection, testing, and analysis that provide insight to the effect of precipitation hardening on the strength of a weld for a given set of SR-FSW process parameters. Specifically, this work provides value to the engineers at NASA by predicting the strength contribution of temperature-dependent precipitates spatially with the welded joint. It predicts this by first estimating the relative contributions of solid solution, grain size, and grain orientation strengthening. By quantifying the effects of precipitation hardening, the overall strength of the weld may be better predicted. Ultimately, the quantified effects will be used to calibrate an overarching model that may be used to predict the temperature distribution spatially within a SR-FSW. To aid in the development of this tool, the following topics have been reviewed: (1) the selection of AA2219-T87, (2) the mechanics of precipitation strengthening, (3) the manufacturing

technique of self-reacting friction stir welding, (4) the methods used to strengthen alloys, and (5) the background and techniques of various fracture mechanics testing methods.

## 2.2 Description of AA2219-T87

The 2000-series aluminum alloys are commonly used in aerospace structures due to their strength-to-weight ratio and relatively high fracture toughness. The aluminum alloy AA2219-T87 is an age hardenable alloy widely used in the construction of liquid cryogenic rockets. This alloy comprises a large portion of NASA's SLS rocket, as well as previous launch vehicles including Saturn V and Space Shuttle. It is particularly favored due to its weldability, high strength to weight ratio, and superior oxidation and corrosion resistance (Elangovan, 2007). The nominal chemical composition is shown in Table 2.1. The T87 condition indicates that the material was solutionized at 535°C, strain hardened by 7%, and then aged for 18 hours between 170°C and 180 °C (Papazian, 1982).

Table 2.1. AA2219-T87 nominal chemical composition (Buccio, 1993).

Al	Cu	Fe	Mg	Mn	Si
bal.	5.8-6.8	0.3 max	0.02 max	0.2-0.4	0.2 max
Ti	V	Zn	Zr	Residuals	
0.02-0.10	0.05-0.15	0.1 max	0.1-0.25	0.15 max	

## 2.3 Precipitate Strengthening

AA2219 is a precipitate strengthened alloy with precipitates that evolve as a function of temperature and time. Plastic deformation in the material is slowed by dislocation interactions with the precipitated particles (Dieter, 1986; Ashby, 2009). The dislocations are obstructed by both particle shearing and Orowan looping, depicted in Figure 2.1. These types of interactions

are also called cutting stress and bowing stress, respectively, as dislocations will either cut through or bow around individual precipitates.

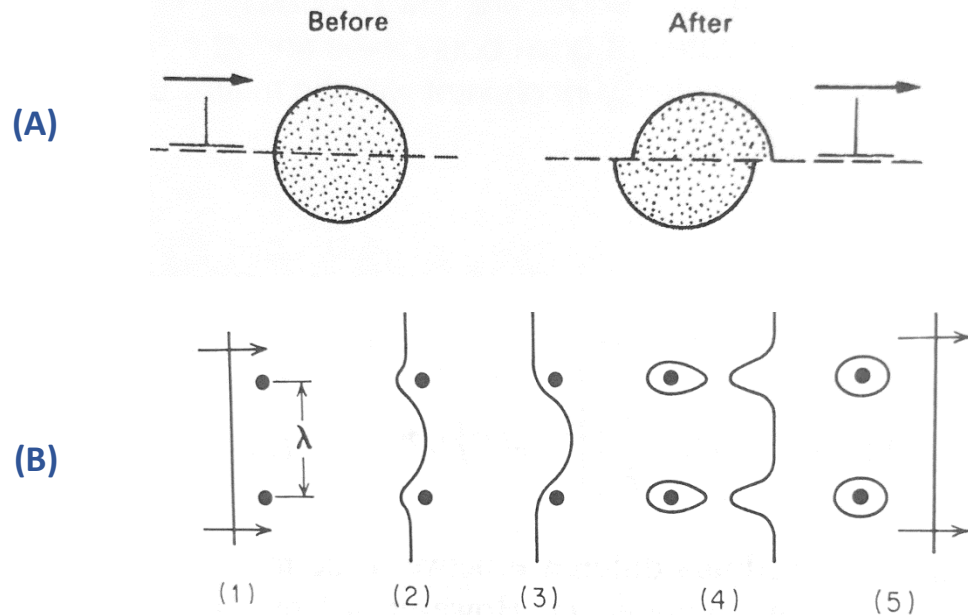


*Figure 2.1. Example of particle shearing (a) and Orowan looping (b) (Ashby, 2009; Dieter, 1986).*

The amount of shearing and looping is based on a number of factors including particle size and spacing. Generally, when precipitates are relatively small and equally spaced throughout the alpha matrix, particle shearing occurs. As the bulk of precipitates grow larger and become more dispersed, Orowan looping occurs. To achieve a high strength, precipitate strengthened alloy, it is advantageous to maximize the number of small precipitates and encourage particle shearing. As the material is over-aged and particles increase in size and spacing, the strength will decrease (Porter, 1981). These relationships are shown in Figure 2.2 for an Al-4 wt% Cu alloy that has been aged at 150°C (Ashby, 2009).

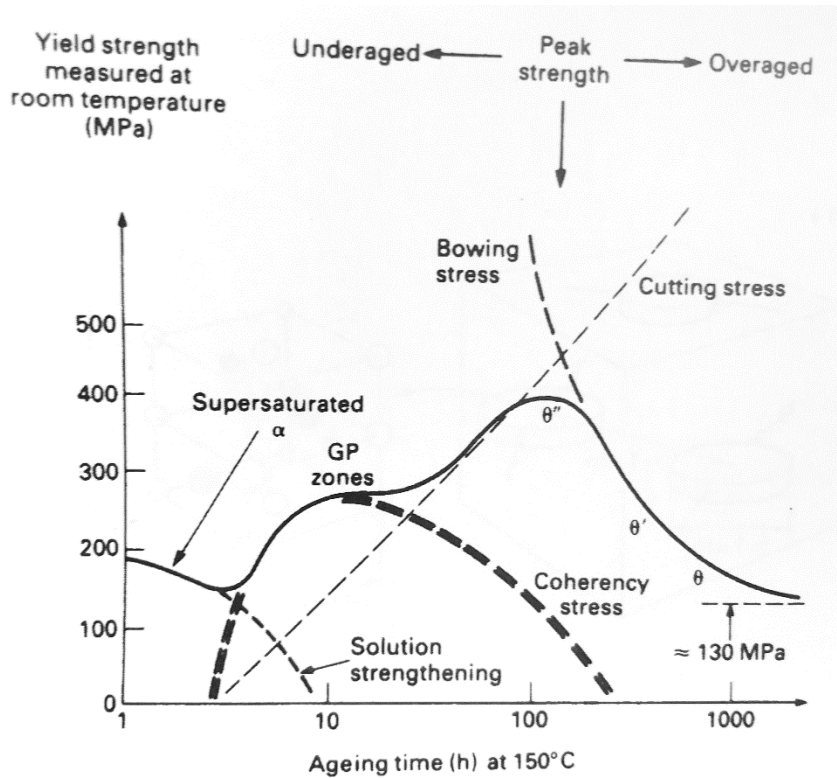


*Figure 2.2.* The relationship between aging and yield strength for an Al-4 wt% Cu alloy (Ashby, 2009). Note the cutting stress and bowing stress lines.

Precipitate phase evolution is as follows: Guiner-Preston zones (GPI and GII)  $\rightarrow \theta'$   $\text{CuAl}_2 \rightarrow \theta \text{ CuAl}_2$ . GPI and GII zones, also known as  $\theta''$  phases, are disk-like precipitates ranging in size from 1 atom to 3 nm thick and 2 to 30 nm in diameter. As aging occurs, unstable GPI and GII zones begin to dissolve and metastable  $\theta'$  phases begin forming. The  $\theta'$  phases are larger disk-like precipitates on the order of 5 to 50 nm thick and 30 to 250 nm in diameter. Finally, as more time passes and higher temperatures are reached,  $\theta'$  phases dissolve and stable  $\theta$  phases form. These large  $\theta$  phase agglomerations are spherical ranging 1 micron and larger in diameter. Note that phase transformation occurs as a function of temperature and time. In which case, phase transformation may occur over time as a function of a single temperature.

The kinetics of the phase transformation are primarily temperature dependent. Calorimetric data taken from literature (Papazian, 1982) provides insight on the precipitation kinetics of this

alloy. The differential heat capacity versus temperature data of (Papazian, 1982) are provided in Figure 2.3 for a heating rate of 20 K/min. The data represent the change in energy of the system as phases are formed and depleted. The data indicate that GP zone dissolution (blue shaded region) occurs between 100 and 200 C, at which point  $\theta'$  formation takes place (green shaded region). The  $\theta'$  phases in existence begin to dissolve at 300C (purple shaded region). Stable  $\theta$  phases are expected to form between 400 and 450°C (red shaded region).

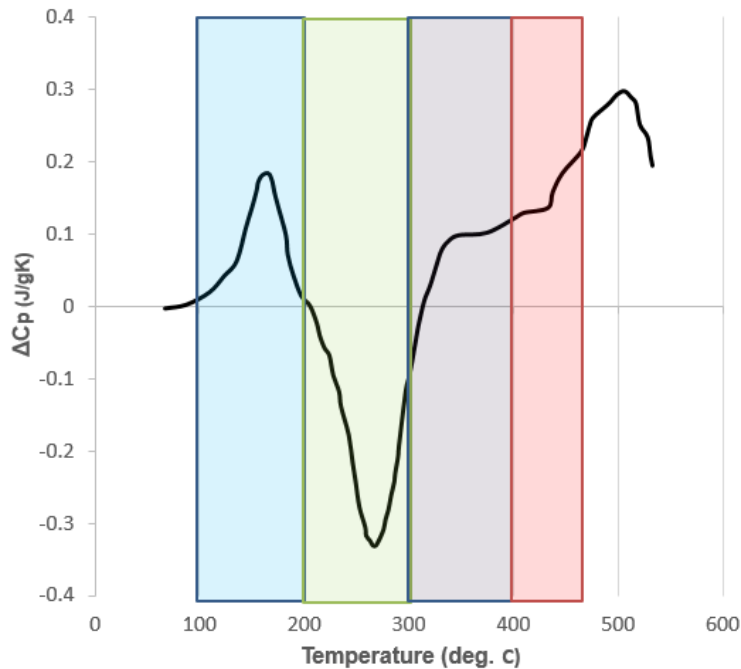


*Figure 2.3.* Calorimetric data found in literature (Papazian, 1982).

## 2.4 Self-Reacting Friction Stir Welding

Friction stir welding is a solid state joining process that utilizes friction-generated heat and large-scale shear to mechanically mix/join materials. The traditional friction stir weld (FSW) is created by use of a FSW tool and backing anvil or reaction plate. The FSW tool consists of a pin that penetrates the material to near through-thickness, and a crown shoulder. The primary function of the pin portion of the tool is to mechanically mix the weld zone (nugget or stir zone), while the primary function of the shoulder is to generate heat from friction. The traditional FSW

process requires that the base material be rigidly clamped to a reaction plate. The FSW is then achieved by first spinning the FSW tool to a desired rotational speed. Next, the tool pin is plunged into the material to be welded. The tool is plunged into the base material by use of either a displacement control or load control command. Regardless of the control signal, the FSW tool crown shoulder is pressed against the base material while the tool spins, thereby generating frictional heat. The stationary reaction anvil reacts and “grounds” all plunge forces required to create the weld. Finally, while maintaining a consistent rotational rate and plunge command, the FSW tool is traversed along the length of the weld at a prescribed translational speed. The primary process parameters of interest include: tool rotational speed ( $\omega$ ), tool translational speed ( $v$ ), crown plunge force ( $F_{crown}$ ), and tool tilt angle ( $\varphi$ ).

The self-reacting friction stir weld process differs from the traditional process in that it employs a mobile reaction anvil. The SR-FSW tool consists of three individual components: the pin, the root shoulder (and retaining nut), and the crown shoulder. A schematic of a generic SR-FSW tool is provided in Figure 2.4.

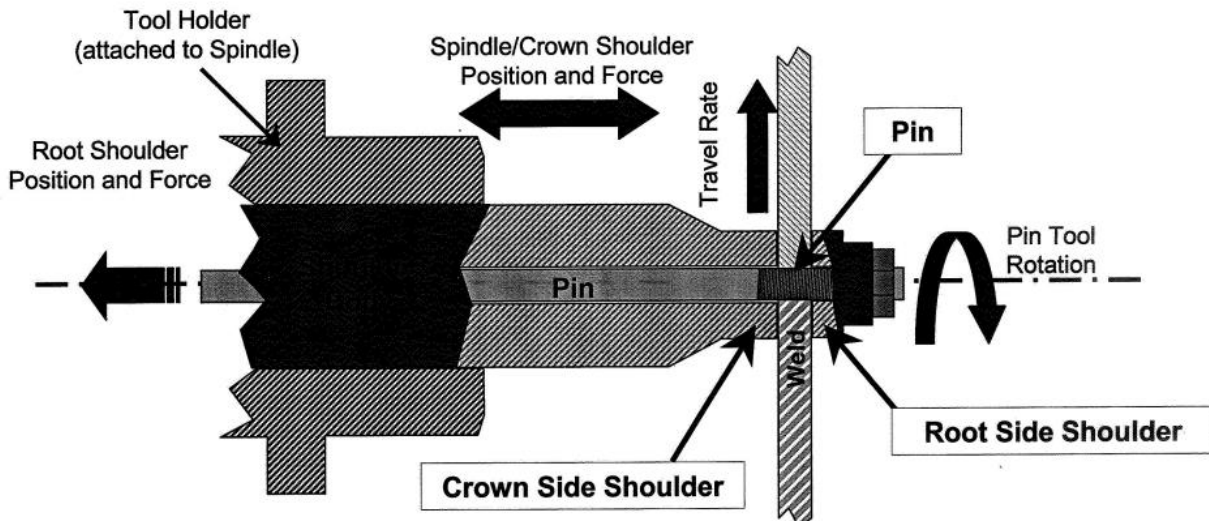


*Figure 2.4. Schematic of a generic SR-FSW tool and the tool-material interaction (Bjorkman, 2003).*

The SR-FSW tool is assembled in such a way that the pin, root shoulder, and retaining nut are all controlled as a single unit. In which case, the SR-FSW process utilizes the root shoulder as the weld reaction anvil. This enables circumferential welds, as example, to be produced by use of this method. The primary weld process parameters to be specified in the SR-FSW process include: the tool rotational speed, the tool translational speed, the crown plunge force, the root/pin reaction force, and tool tilt angle. Though both the traditional and self-reacting friction stir welding processes are performed below the melting temperature of the base material, the weld temperatures induced in AA2219 may reach as high as the precipitate melting temperature (~550°C). Therefore, optimization of the weld process parameters is essential to ensure the appropriate material microstructure.

## 2.5 Strengthening Mechanisms Manifesting in Crystalline Solids

The model/tool presented later in this work quantifies the relationship between the ultimate tensile strength UTS and the strengthening mechanisms observed in SR-FSW AA2219. It is commonly understood that the plastic deformation of crystalline metals is primarily caused by the movement of dislocations (Ashby, 2009). Methods have been devised to impede the motion of these dislocations in order to increase the strength of a material. The following strengthening approaches are commonly implemented within crystalline metals: solid solution strengthening, grain boundary strengthening, grain size strengthening, grain orientation strengthening, precipitate strengthening, point defect strengthening, and strengthening from cold working (Dieter, 1986).

As this work is focused on 2000-series aluminum alloys, and minimal point defects exist in this family of alloys, point defect strengthening is not considered here. Likewise, no intergranular fracture is observed in the base material or weld zones studied, so no grain

boundary strengthening will be included in this work. Furthermore, any strengthening benefits from base material cold working would be mitigated by the SR-FSW process, as temperatures over half of the homologous temperature are reached. Thus, this section focuses on the following strength mechanisms for processed AA2219 to be included in the presented model: solid solution strengthening, grain size strengthening, grain orientation strengthening, and precipitation strengthening.

### 2.5.1 Measurement of Strength

The ultimate tensile strength of the material is approximated by use of microhardness data for the remainder of this work. In many alloys including AA2219, there is a linear relationship between the UTS and microhardness (Tiyakioglu, 2015). The relationship is shown in Figure 2.5. Included is data found in literature combined with experimental data from this work and a trend line fitted to the data. It was outside the scope of this project to recreate the work performed by Raza, but a single experimental data point was included to validate his work.

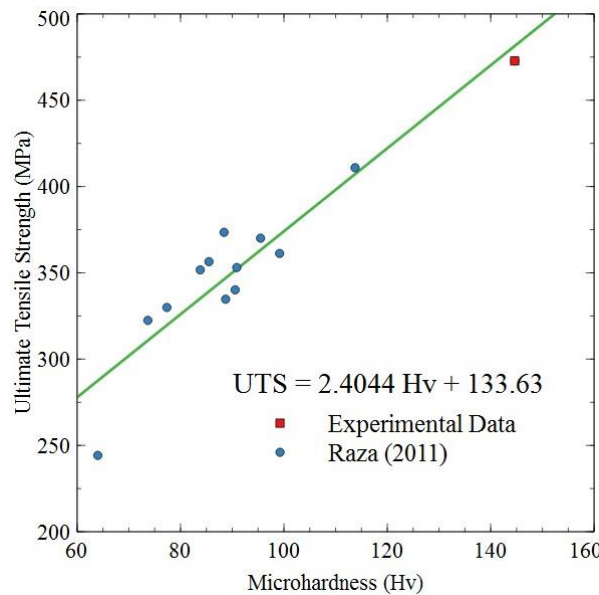


Figure 2.5. Relationship between microhardness and UTS for AA2219 (Raza, 2011).

### 2.5.2 Solid Solution Strengthening

Solid solution strengthening is a common form of hardening for alloys that occurs when secondary elements dissolve into the material matrix. The solute element's atoms then interact with dislocations, impeding dislocation movement and causing an increase in material strength. Thus, the solid solution strength will increase as the number of solute atoms available in the matrix increases (Ashby, 2009).

The alloy AA2219 derives a portion of its strength from solution hardening. The elements of interest are aluminum (matrix) and copper (solute). Given that the atomic radii of copper is roughly the same size as aluminum, substitutionary solid solution strengthening will occur, meaning copper atoms will replace aluminum atoms with the FCC crystal structure (Dieter, 1986). Upon aging the material, either by time or heat treatment, the Cu and Al atoms will diffuse together to form  $\text{Al}_2\text{Cu}$  precipitate phases following the sequence discussed in Section 2.3 (Guiner-Preston zones (GPI and GII)  $\rightarrow \theta'$   $\text{CuAl}_2 \rightarrow \theta$   $\text{CuAl}_2$ ). The type of precipitate formed during this process is dependent on the thermal history of the material.

### 2.5.3 Grain Size Strengthening

The Hall-Petch relationship expresses the grain-size dependence of the material's strength as a function of the grain size and relative grain boundary hardening. Its strengthening effect ( $\Delta\sigma_{UTS}$ ) is defined in

$$\Delta\sigma_{UTS} = \sigma_0 + \frac{k}{\sqrt{d}} \quad (2.1)$$

where  $\sigma_0$  is the friction stress which defines the overall resistance to the movement of dislocations within the crystal lattice,  $k$  is the locking parameter which quantifies the relative

hardening of grain boundaries, and  $d$  is the grain diameter of an equiaxed grain (Dieter, 1986).

The constant  $\sigma_0$  is equal to 20 MPa and  $k$  is equal to 0.4 MPa/m (Hansen, 2004).

For materials with elongated grains, such as that observed in wrought AA2219-T87, there is a method for calculating an average grain diameter. The average diameter of elongated grains is defined in

$$\bar{d} = V^{\frac{1}{3}} = \left( \frac{\pi d^2 h}{4} \right)^{\frac{1}{3}} \quad (2.2)$$

where  $d$  and  $h$  are the diameters of the grain in the transverse and elongated directions, respectively (Vajtai, 2013). This equation determines the average diameter of a grain based on the volume of cylinder.

#### 2.5.4 Grain Orientation Strengthening

If grains are oriented in directions that encourage slip, the strength of the material will be affected. Specifically, when a series of grains are oriented for easy slip, the material's critically resolved shear stress (CRSS) will be reached with minimal external energy input. This results in a lower UTS than a material with a series of grains with no orderly orientation. The inverse of this is true, such that if grains are oriented such that large amounts of external energy are needed to reach the CRSS, the UTS of the material will be higher.

Literature predicts that there is a 40% difference in yield strength between crystals oriented in the strongest and weakest directions (Hutchison, 2015). Because this is such an extreme case, Hutchison notes that the yield strength effects seen on the macroscale of a textured material will generally be significantly lower. Literature also suggests that the difference in UTS

between crystals oriented in the strongest and weakest directions to be half of the difference observed for the yield strength (Dieter, 1986). This relationship is expressed in Equation 2.3.

$$\frac{\sigma_{UTS}(\text{grain orientation max})}{\sigma_{UTS}(\text{grain orientation min})} \sim 20\% \quad (2.3)$$

If it is believed that AA2219 consists of randomly oriented grains, one should expect to experience somewhere between the maximum and minimum grain orientation ultimate tensile strengths. Thus, the total contribution of grain orientation to strengthening can be expressed using an upper and lower bound as

$$\Delta\sigma_{UTS \text{ grain orientation}} = \pm 10\% \Delta\sigma_{UTS \text{ solid solution}} \quad (2.4)$$

### 2.5.5 Precipitate Strengthening

The details of the precipitation hardening mechanics are discussed in more detail in Section 2.3. However, in this section the methods for calculating the effects of precipitation hardening on the UTS of a material are presented. The strength contribution for plate-like precipitates, such as GPI and GII zones and theta-prime phases, are given in (Kelly, 1972)

$$\Delta\sigma_{UTS \text{ plates}} = \frac{0.85Gb}{2\pi(1-\nu)^{1/2}} \frac{C}{D} \ln\left(\frac{2D}{\pi r_0}\right) \quad (2.5)$$

where  $G$  is the shear modulus ( $G=26$  GPa),  $b$  is the Burgers vector ( $b=2.84E-10$  m),  $\nu$  is the Poisson's ratio ( $\nu=0.3$ ),  $D$  is the disk diameter,  $r_0$  is the dislocation core radius ( $r_0=6E-10$  m),  $t$  is the plate/disk thickness, and  $C$  is given by

$$C = \sqrt{f \frac{D}{t} + \left(\frac{2}{\pi} - \frac{\pi t}{2D}\right) f \frac{D}{t}} \quad (2.6)$$

where  $f$  is the volume fraction of precipitates. The strengthening effects for spherical precipitates, such as the larger theta phase agglomerations are given in (Dieter, 1986)

$$\Delta\sigma_{UTS \text{ sphere}} = \frac{0.13Gb}{\lambda} \ln\left(\frac{r}{b}\right) \quad (2.7)$$

where  $r$  is the particle radius,  $\lambda$  is the particle spacing, and all other variables are defined above. As the sizes and volume fraction of precipitates in existence are not quantified for the material, these equations are not implemented into the model presented in this work. They have, however, been included in this section for completeness.

## 2.6 Fatigue Crack Growth Testing

A fatigue crack growth test measures the resistance of a material to extend a crack during cyclic loading. It is based upon the concept that the number of cycles needed to grow a crack to a specified length can be predicted. Inspection intervals can be set if the crack growth rate is known for cracks of a detectable size. This allows critical parts to be repaired prior to any catastrophic damage to the structure. This damage tolerance approach to fatigue is heavily used in the aerospace community.

There are three methods by which a crack extends, shown in Figure 2.6. Most common in fracture mechanics is Mode I which is also known as the opening mode. Mode II is considered in-plane shearing and Mode III is considered tearing or out of plane shearing.

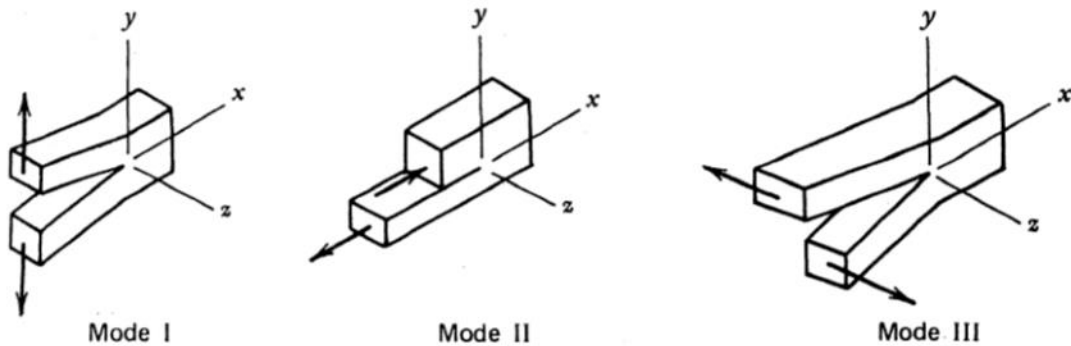


Figure 2.6. Loading modes for a crack (Stephens, 2001).

The stress intensity factor  $K$  defines the state of stress near the crack tip. It is dependent upon the magnitude of nominal stress, crack size and shape, and sample geometry. It provides a way for the intensity of stress near a crack tip to be quantified and compared regardless of sample geometries (Broek, 1983). Likewise, the stress intensity factor range,  $\Delta K$ , defines the change in the stress intensity during fatigue loading

$$\Delta K = K_{max} - K_{min} = f(a)\Delta\sigma\sqrt{\pi a} \quad (2.8)$$

where  $f(a)$  is the geometry factor,  $\Delta\sigma$  is the change in stress, and  $a$  is the crack length. Values of the stress intensity factor and stress intensity factor range are typically determined using analytical or numerical calculations based upon the theory of elasticity (Anderson, 2005).

The crack growth rate,  $da/dN$ , is calculated by taking the derivative of crack length  $a$  with respect to the number of cycles  $N$ . Numerical differentiation is susceptible to error when noisy data is considered. Two common methods given in ASTM E647 for obtaining  $da/dN$  are the secant method and the incremental polynomial method. While the traditional secant method simply calculates the slope of two adjacent points on an  $a$  vs.  $N$  curve, it typically exhibits larger amounts of scatter than the incremental polynomial method, which fits second-order polynomials to  $a$  vs.  $N$  data. Another numerical method to calculate  $da/dN$  is the central finite difference method given by

$$\frac{da}{dN} = \frac{a_{i+1} - a_{i-1}}{N_{i+1} - N_{i-1}}. \quad (2.9)$$

The crack growth rate curve can be created by plotting the log  $da/dN$  on the ordinate axis and the log  $\Delta K$  on the abscissa, shown in Figure 2.7. There are three regions of the crack growth rate curve that characterize the behavior of the material. They are as follows: (I) near-threshold growth, (II) stable crack growth, and (III) unstable crack growth.

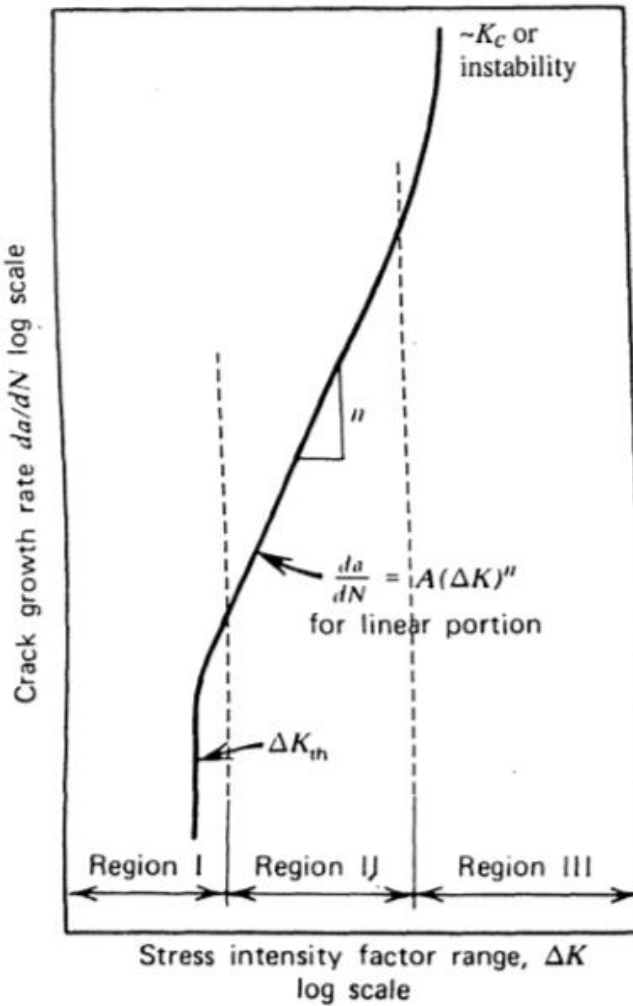


Figure 2.7. Schematic of fatigue crack growth behavior and corresponding regions of crack growth (Stephens, 2001).

The lower  $\Delta K$  portion or Region I of the curve, indicates the threshold value  $\Delta K_{th}$ .

According to ASTM E647, the threshold occurs around crack growth rates of  $10^{-10}$  m/cycle.

Typically, no crack propagation is observed below this value. Typically, microstructural effects heavily influence the behavior of cracks in this region, along with mean stress, frequency, and loading effects.

Region II, or the Paris Region of crack growth, is characteristic of stable crack growth that experiences a power law relationship between  $\log da/dN$  and  $\log \Delta K$ . The Paris equation is given by

$$\frac{da}{dN} = A(\Delta K)^n \quad (2.10)$$

where  $A$  and  $n$  are material constants used to determine the crack growth resistance of a material. Typically, crack propagation in the Paris region is controlled by environmental effects and is not heavily influenced by microstructure as in Region I.

Region III behavior is commonly ignored in damage tolerant design because it minimally affects the total life of a part. This is because the number of cycles spent in this region is significantly smaller than those spent in Regions I and II. Some correlate a material's fracture toughness ( $K_C$ ) value to the point of instability in the crack growth rate curve (Bannantine, 1990).

Differences in fatigue behavior in the Paris region can often be attributed to crack closure effects (Suresh, 1998). This phenomenon was first observed by Elber who observed that fatigue cracks would close despite there being a remotely applied tensile load. He suggested that crack closure reduced the crack propagation rate by decreasing the effective stress intensity factor range,  $\Delta K_{eff}$ , which is defined by

$$\Delta K_{eff} = K_{max} - K_{op} \quad (2.11)$$

where  $K_{max}$  is the maximum stress intensity factor when the crack is fully opened and  $K_{op}$  is the stress intensity factor when the crack first opens. When crack closure is present,  $K_{op}$  is greater than  $K_{min}$ . Crack closure in dry, inert environments can occur as a result of crack tip plasticity (plasticity induced crack closure) and fracture surfaces coming in contact with one another (roughness induced crack closure) (Anderson, 2005). In plasticity induced crack closure (PICC)

a plastic zone is developed at the crack tip where the yield stress is exceeded. Once the crack has grown through the plastic zone, the residual plastic deformation remains as part of the plastic wake behind the crack tip. This plastic wake causes a decrease in crack growth rate. This type of crack closure is common in ductile materials. When a crack experiences roughness induced crack closure (RICC), a mix of Mode I and Mode II loading at the crack tip due to a kinked crack causes the asperities in the wake of the crack to make contact, decelerating the rate at which the crack grows. PICC and RICC are illustrated in Figure 2.8.

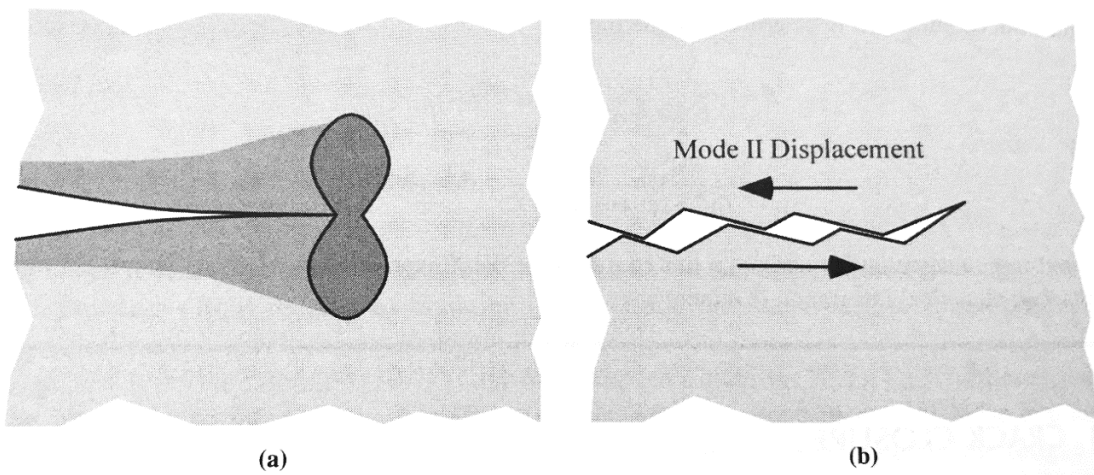


*Figure 2.8. Illustration the crack faces during (a) PICC and (b) RICC (Anderson, 2005).*

Fatigue crack growth testing practices are defined by ASTM E647 Standard Test Method for Measurement of Fatigue Crack Growth Rates. The standard can be applied from near-threshold to  $K_{max}$  controlled instability testing. The standard compact tension (C(T)) specimen used for testing is shown in Figure 2.9.

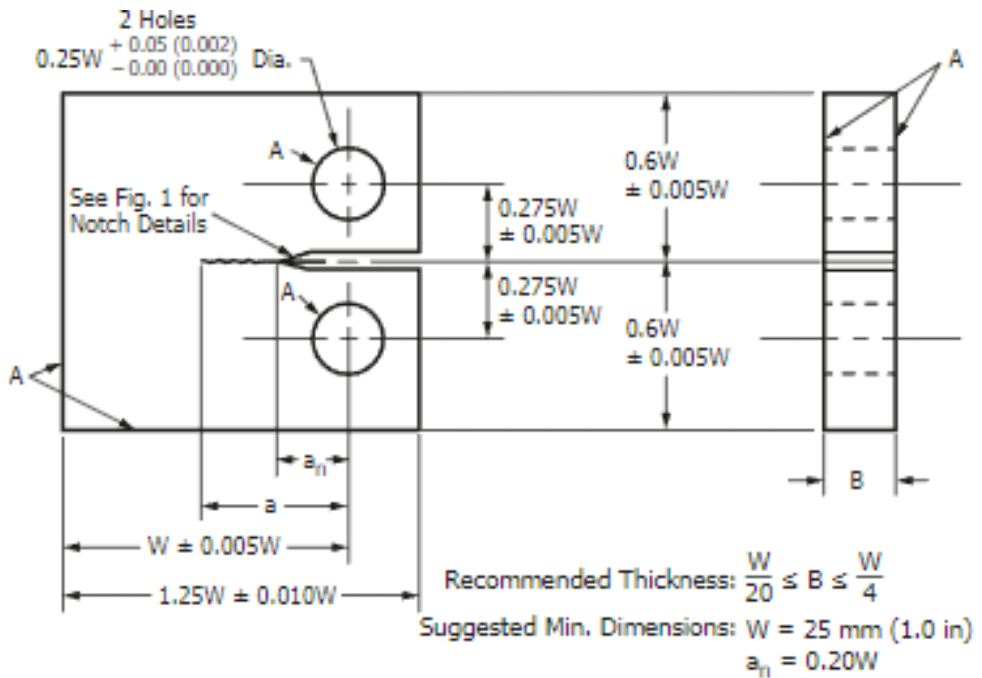


Figure 2.9. Standard dimensions of C(T) sample per ASTM E647. Dimensions in millimeters (inches).

The following is a summary of the test procedure used in this work:

- Fatigue precracking is performed such that the final  $K_{max}$  during precracking does not exceed the initial  $K_{max}$  of testing.
- Once the fatigue precrack reaches the greater of  $0.10b$ ,  $h$  or 1.0 mm, fatigue precracking is ended, and the machine is paused, where  $b$  is the thickness of the sample and  $h$  is the height of the notch.
- The crack length is verified using a non-destructive, quick curing, silicone rubber compound to create a replica of the surface. An optical microscope is used to measure the length of the surface replica of the crack.
- Testing is resumed. Load, displacement, and cycle data are recorded continuously throughout the test.
- Testing is complete once the crack reaches  $a/w > 0.8$ .

Upon completion of testing, the normalized crack length,  $a/W$ , for the specific specimen geometry is determined by the equation given in the standard and below as

$$\alpha = \frac{a}{W} = c_0 + c_1 u_x + c_2 u_x^2 + c_3 u_x^3 + c_4 u_x^4 + c_5 u_x^5 \quad (2.12)$$

where the constants  $c_0$  through  $c_5$  are given in the E647 standard for compliance measurements taken from the tip of the CMOD ( $V_o$ ).  $U_x$  is given by

$$u_x = \left\{ \left[ \frac{EvB}{P} \right]^{\frac{1}{2}} + 1 \right\}^{-1} \quad (2.13)$$

$\Delta K$  is then calculated by the equation given in the standard

$$\Delta K = \frac{\Delta P}{B\sqrt{W}} \frac{(2 + \alpha)}{(1 - \alpha)^{\frac{3}{2}}} (0.886 + 4.64\alpha - 13.32\alpha^2 + 14.72\alpha^3 - 5.6\alpha^4) \quad (2.14)$$

where  $E$  is the elastic constraint modulus,  $B$  is the specimen thickness, and  $v/P$  is the compliance for a given cycle. The elastic constraint modulus is used as a factor to correct compliance measurements to the physical crack length measured during testing. In the absence of all error,  $E$  is the Young's modulus for the material. The equation for  $\Delta K$  has been determined by use of FEA for the standard C(T) sample as well as various other common specimen geometries. As previously mentioned,  $da/dN$  can be calculated using the secant, incremental polynomial, and central finite difference methods.

## 2.7 Fracture Toughness Testing

Fracture toughness testing measures the resistance of a material to extend a crack under quasi-static loading (Anderson, 2005). Plane-strain fracture toughness, also referred to as  $K_{IC}$ , testing methods are outlined in ASTM E399, where it is assumed that a material behaves in a

predominantly linear-elastic, plane-strain condition prior to failure, with the plastic zone size at the crack tip small relative to the overall sample geometry.

Fracture mechanics theory is based upon the assumption that cracks are infinitely sharp. Thus, there are stringent precracking procedures outlined in E399 to ensure repeatability in test results between laboratories. Those requirements are included in the testing procedure below.

The following is a summary of the test procedure and in this work:

- Fatigue precracking is initiated at a constant amplitude load such that the final  $K_{max}$  achieved during precracking does not exceed  $0.6K_{IC}$  for the expected fracture toughness value.
- Once the fatigue precrack reaches  $0.45W$  to  $0.55W$  fatigue precracking is ended, and it is assumed that a sharp crack exists in the sample.
- The crack length is verified using a non-destructive, quick curing, silicone rubber compound to create a replica of the surface. An optical microscope is used to measure the length of the surface replica of the crack.
- The  $K_{IC}$  test begins. A loading rate between  $0.33$  and  $1.67$  kN/s is applied to the sample. Load and displacement data are digitally recorded throughout the test until the sample fails.

Upon completion of the test, the load and displacement data are plotted as shown in Figure 2.10. There are three different possible outcomes for the data, which is used to determine the conditional value of  $P_Q$ . The  $K_{IC}$  value for the material is later determined from  $P_Q$ .

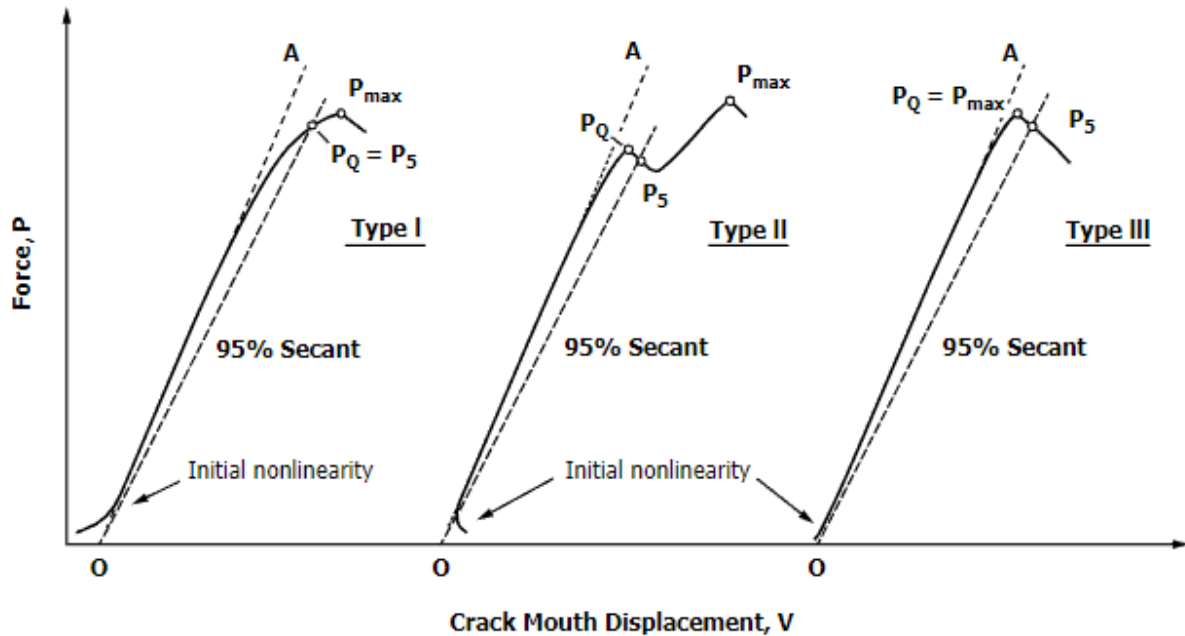


Figure 2.10. Method of determining  $P_Q$  from load and displacement data from a  $K_{IC}$  Test (ASTM E647).

The value of  $P_Q$  and its corresponding CMOD value are used in Equations 2.12 and 2.13 to calculate the crack length of the sample at the point. Finally, the crack length and  $P_Q$  are applied to the equation for a provisional  $K_Q$  of a standard compact tension sample given by

$$\Delta K_Q = \frac{P_Q}{B\sqrt{W}} \frac{(2+\alpha)}{(1-\alpha)^{\frac{3}{2}}} (0.886 + 4.64\alpha - 13.32\alpha^2 + 14.72\alpha^3 - 5.6\alpha^4). \quad (2.15)$$

If the following standards for the data are met,  $K_Q$  is considered the  $K_{IC}$  property of the material:

$$0.45 \leq \alpha \leq 0.55 \quad (2.16)$$

$$w - a \geq 2.5 \left( \frac{K_Q}{\sigma_{YS}} \right)^2 \quad (2.17)$$

$$P_{max} \leq 1.10P_Q. \quad (2.18)$$

## CHAPTER 3 VIRGIN MATERIAL CHARACTERIZATION

### 3.1 Introduction

This work provides NASA a better understanding of the microstructure and properties of SR-FSW AA2219-T87 joints through the collected experimental data. AA2219-T87 is the primary alloy used in the construction of the core stage and upper stage of NASA's Space Launch System rocket (Vickers, 2016). The local strength of the material varies significantly as it undergoes the SR-FSW process. The welding effect causes the welded assembly to behave as a composite material of varying microstructure. As such, this chapter provides insight to the base material's phase transformation kinetics and grain size.

### 3.2 Material Selection

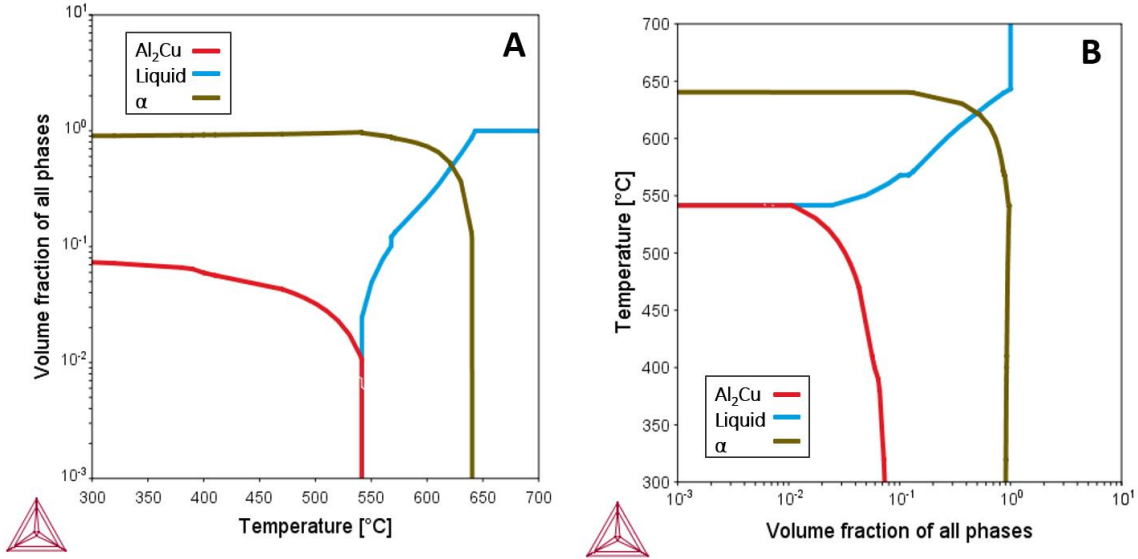
All material used for this study was sourced from a single lot of AA2219-T87. The aluminum was purchased in plate form having thickness of 19.05 mm (0.75"). The materials nominal chemical composition is provided previously in Table 2.1. The exact chemical composition was not measured in this work. Table 3.1 provides the tensile properties for the virgin (T87) and annealed (O) material found in literature (ASM, n.d.).

Table 3.1. *Tensile properties for AA2219* (ASM, n.d.).

Aging Condition	$\sigma_y$ (MPa)	UTS (MPa)	Elongation to Failure
T87	393	476	10%
O	75.8	172	18%

### 3.3 Property Diagram

Phase volume fraction diagrams were created for the AA2219-T87 alloy by use of Thermo-Calc software. The maximum allowable composition for each alloying element were used to produce the plots. The diagrams provide information about the relative volume fraction of the  $\alpha$ ,  $\text{Al}_2\text{Cu}$ , and liquid phases as a function of temperature. While not a typical phase diagram, the volume fraction diagram provides insight to both the relative amounts of phases in the material as well as the rates of phase change. Though Figures 3.1(a) and 3.1(b) provide the identical information, they are provided with transposed axis for ease of use. The data in Figure 3.1 indicates that the eutectic temperature is roughly 550 °C. Below this temperature, one could use Figure 3.1(b) to determine the volume fractions of  $\alpha$  and  $\text{Al}_2\text{Cu}$ . The figures indicate that at 500°C the material would consist of approximately 3%  $\text{Al}_2\text{Cu}$  and 97%  $\alpha$ . Furthermore, the slope of the red  $\text{Al}_2\text{Cu}$  volume fraction line indicates that the rate of  $\text{Al}_2\text{Cu}$  dissolution is relatively stable at temperatures below approximately 400°C, and increases sharply at temperatures between 400°C and 550°C. At and above the eutectic temperature the  $\text{Al}_2\text{Cu}$  phase is no longer in existence and the material is characterized as a supersaturated aluminum. At the eutectic temperature the copper is diffused back into the alloy system creating a solid solution. If the material is quickly cooled from solid solution, any copper that may contribute to metastable strengthening phases is transferred back into the super saturated aluminum matrix. However, if the material is slowly cooled from the elevated temperatures, over-aging occurs. This results in the remaining copper being effectively locked in non-strengthening, stable, theta phases. The volume fraction diagrams presented here were used during design-for-experiment exercises and data interpretation for this work.



*Figure 3.1.* Property diagram of AA2219-T87 generated for maximum allowable chemical composition of all alloying elements.

While temperatures near 550 °C are likely experienced in the stir zone, lower temperatures are experienced in the TMAZ and HAZ of the weld. Given the unstable nature of the primary strengthening phases (GP zones), microstructural evolution will occur in the stir zone as well as the TMAZ and HAZ. In which case, the strengthening precipitate evolution will be spatially dependent. In order to quantify the microstructural strength of the weld, the growth and dissolution of GP zones and θ phases at various temperatures must be better understood.

### 3.4 Phase Transformation Kinetics

Square samples (minimum size: 10 mm by 10 mm by 5 mm thick) were sectioned from the base material for isothermal stress-free aging studies. Samples were ground for 3 minutes per step using successively finer SiC paper (240 grit, 600 grit, 800 grit, followed by 1200 grit SiC). The samples were then polished using 3 µm diamond suspension and 1 µm diamond suspension for 3 minutes per step, and 0.4 µm colloidal silica suspension for 90 seconds. All grinding and polishing steps were performed with a 3-pound force with disc and holder rates of

250 and 120 rpm. Triplicate specimens were placed in a temperature-stabilized furnace for a predetermined period of time, removed, and allowed to cool in ambient conditions to room temperature. The samples were then cold mounted in epoxy resin and again ground, and polished following the schedule detailed above. Microhardness mapping was subsequently performed on all samples in order to characterize the material evolution as a function of temperature exposure. An array of (10x10) indents was created for each sample. A single indent force was used for each specimen and was selected based upon optimum indent measurements. Indent array spacing was again set at 2.5 times the optimal indent size for each specimen in order to maximize data collection fidelity.

Microhardness data of non-stressed aged AA2219 samples indicate an evolution in microhardness with exposure time that aligns well with the results of the calorimetric study discussed in CHAPTER 2. As previously discussed, the calorimetric data indicates the temperatures at which phase transformations take place. The measured microhardness versus temperature data collected after 2.8 hours of thermal exposure is provided in Figure 3.2 along the primary y-axis with a comparison to the calorimetric data from Papazian along the secondary y-axis. The error bars for the microhardness points indicate  $\pm 1$  standard deviation of the measurements.

The sets of data indicate that the hardness begins to decrease at the temperature where GP zones dissolve (blue shaded region), followed by a rapid decrease in hardness as the  $\theta'$  phases form (green shaded region) and deplete (purple shaded region) between 200°C and 400°C. No significant change in microhardness is observed after 400C, where large  $\theta$  phases absorb any remaining copper in the material.

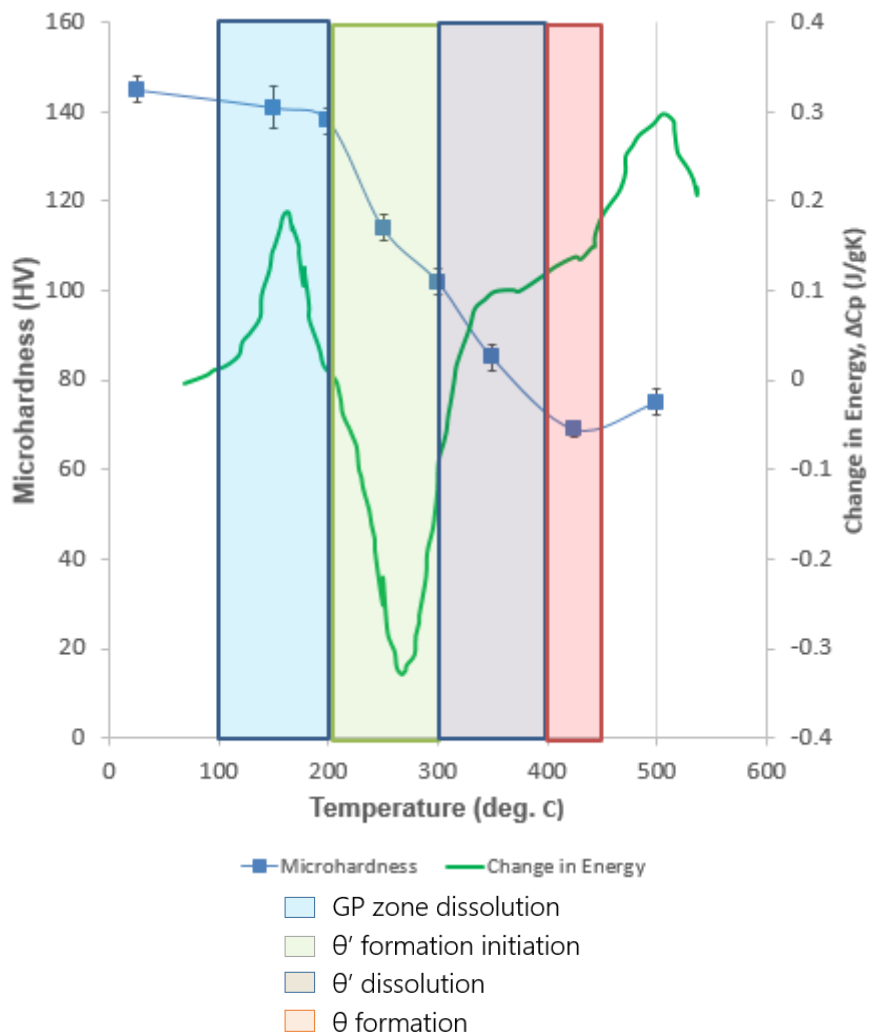


*Figure 3.2.* Non-stressed isothermal microhardness results collected after 2.8 hours of thermal exposure compared to calorimetric data from Papazian.

Microhardness results from the base material (T87) and non-stressed isothermal samples with extended thermal exposure times of 24, 72, and 140 hours were also collected following the same experimental methods as described above. Experimental results are presented in Figure 3.3 with error bars representing  $\pm 1$  standard deviation of the microhardness measurements. The data suggest that all precipitation kinetics occur within the initial 24 hours of exposure for all temperatures above 200°C. Interpretation of the experimental data coupled with the understanding of when phases grow and dissolve from Papazian's calorimetric data indicates that GP dissolution occurs after 24 hours during the 200°C thermal history causing its hardness to

slightly drop from the unaged base material. Furthermore, a mixed microstructure of metastable  $\theta'$  and stable  $\theta$  phases likely exists during the 350°C thermal history. If overaging occurs, as is certainly the case in the 500°C thermal history provided in the figure, all remaining Cu in the alloy will be locked in the stable  $\theta$  phase agglomerations within an hour. As such, it is believed that this value represents the solid solution strength of the alloy tests. The microhardness and corresponding strength for each thermal history is presented in Table 3.2. These estimations are in line with the discussion in (Ashby, 2009).

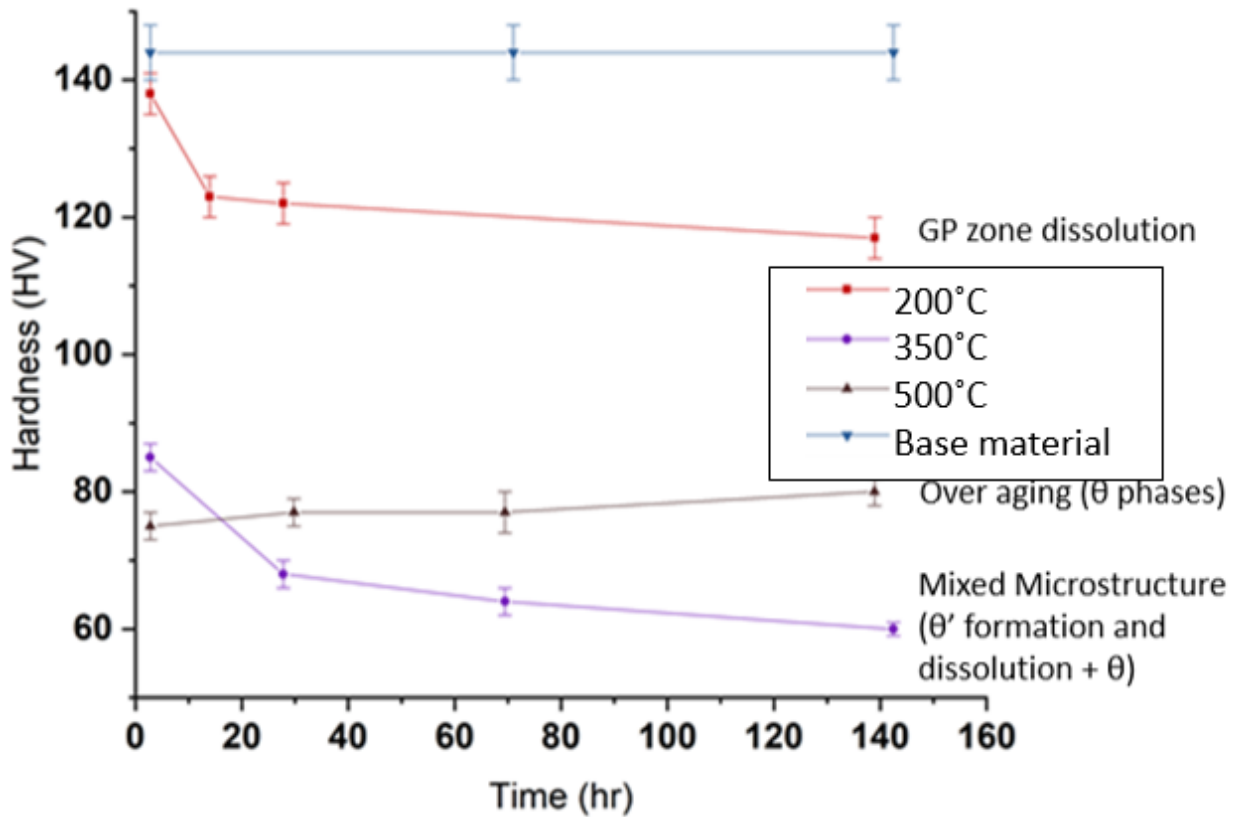


Figure 3.3. Non-stressed isothermal data for multiple thermal histories and the expected microstructures.

Table 3.2. *Expected microstructure and relative strength measurement of three thermal histories.*

Aging Temperature (°C)	Microhardness at 140 hours (HV)	UTS (MPa)	Expected Precipitation Kinetics
200	120	425	GP zone dissolution
350°C	60	300	Mixed Microstructure ( $\theta'$ formation and dissolution + $\theta$ )
500°C	80	250	Over aging ( $\theta$ phases)

### 3.5 Grain Size

Microstructural characterization was performed by use of light optical and scanning electron microscope techniques. Samples were ground for 3 minutes per step using successively finer SiC paper (240 grit, 600 grit, 800 grit, followed by 1200 grit SiC). The samples were then polished using 3  $\mu\text{m}$  diamond suspension and 1  $\mu\text{m}$  diamond suspension for 3 minutes per step, and 0.4  $\mu\text{m}$  colloidal silica suspension for 90 seconds. All grinding and polishing steps were performed with a 3-pound force with disc and holder rates of 250 and 120 rpm. Subsequently, the samples were chemically etched in Keller's reagent for 15 seconds. The materials grain size was measured per ASTM E112 in three perpendicular orientations. The orientations are defined by the normal vector to the plane. They are defined as Longitudinal (L), Transverse (T), and Short (S) and are represented in Figure 3.4. Micrographs of these surfaces can be found in Appendix Figures A.1 to A.3.

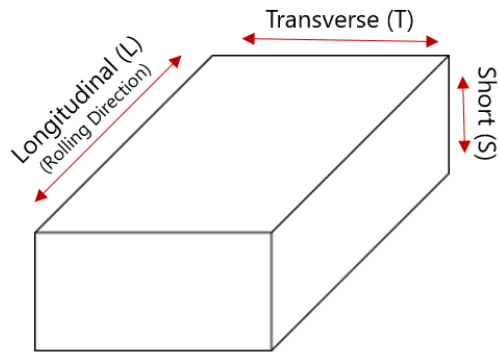


Figure 3.4. Schematic of Longitudinal (L), Transverse (T), and Short (S) directions. The orientation of each plane is defined by the direction normal to the plane of interest.

The grain measurement results for the virgin material are provided in Table 3.3. The horizontal and vertical labels in the table are with respect to the orientation of Figures A.1 to A.3 in the Appendix. It is observed that the grains are elongated in the short and transverse planes along the longitudinal or rolling direction. The grains of the longitudinal plane are relatively equiaxed, indicating that the elongated grains are caused by the rolling operation used to form the plates.

Table 3.3. *Measured grain size for the virgin AA2219-T87.*

Plane	Vertical Grain Size ( $\mu\text{m}$ )	Standard Deviation	Horizontal Grain Size ( $\mu\text{m}$ )	Standard Deviation
S	55.2	6.2	21.6	3.7
L	90.3	14.3	82.7	5.1
T	54.6	5.5	21.9	1.9

The grain measurement results for the isothermal data in the short orientation at 20°C, 150°C, 250°C, 300°C, and 425°C are provided in Table 3.4. Data is collected after 2.8 hours of exposure. Micrographs of the grain sizes are shown in Figures A.4 to A.7 in the Appendix. The measured grain size almost doubles when aged at 300°C, indicating that grain coarsening does occur as a function of temperature in this material. However, when the Hall-Petch relationship

presented in Section 2.5.3 is used to estimate grain size strengthening, there is only a 12% decrease in UTS for the 300°C sample. Thus, a change in UTS measured only from a change in grain size should not be significant.

*Table 3.4. Measured grain size along the longitudinal direction of the short plane for the heat treated AA2219. Data collected after 2.8 hours of exposure.*

Temperature (°C)	Grain Size (μm)	Standard Deviation
20	67.2	3.4
150	95.1	14.8
250	109.9	13.2
300	122.3	26.6
425	119.8	15.6

Additionally, the grain texture was quantified by use of electron backscatter diffraction (EBSD). The EBSD results for the short orientation are provided in Figure 3.5. The results indicate that the plate material has a slight orientation favor towards 001-111 orientation on the short surface. This confirms the discussion of Section 2.5.4 where it is postulated that the material's grains are randomly oriented. As such, the approximation for grain orientation strengthening given in Equation 2.4 applies.

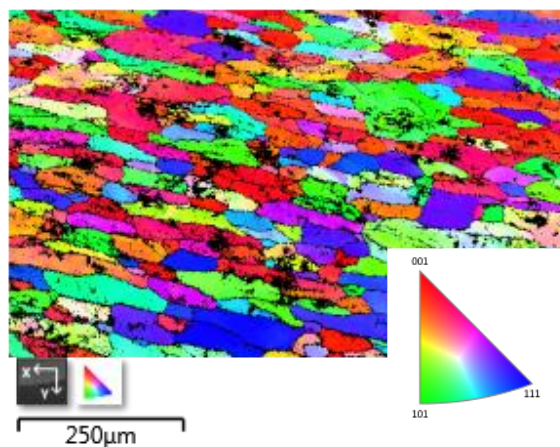


*Figure 3.5. Electron backscatter detector grain orientation map with respect to the short orientation.*

## CHAPTER 4 SELF-REACTING FRICTION STIR WELD CHARACTERIZATION

### 4.1. Introduction

As discussed in CHAPTER 2 of this work, NASA's SLS rocket is manufactured by joining AA2219-T87 panels using the SR-FSW process. The process utilizes large-scale shear and friction to mechanically mix the base material at temperatures below the melting temperature. The solid state FSW process will, however, induce sufficient heat as to affect aging in the base material. Furthermore, the FSW-induced shear will produce a modified grain structure within the weld and the regions adjacent to the weld. This work quantifies the effects of an optimized FSW process on the AA2219-T87 base material. Specifically: (1) residual stresses in the weld are quantified, (2) grain morphology produced by the FSW process is quantified, (3) microhardness is quantified for the base material, weld nugget, and thermo-mechanically affected zone (TMAZ), and heat affected zone (HAZ), (4) the fatigue crack growth rate behavior and fracture toughness values are quantified, and (5) relative amounts of crystalline strengthening mechanisms are postulated spatially as a function of the welding process.

This completed work is meant to provide a better understanding of the microstructure and properties of SR-FSW joints. The remainder of this chapter presents the experimental data collected in this work and discusses the current state of a model and its predictions for the effect of precipitation strengthening on the FSW. Finally, its predictions are discussed relative to the fatigue crack growth behavior.

## 4.2. Welded Material Characterization

The SR-FSWs studied in this work were created by use of pre-defined optimal process parameter set for 15.875 mm (0.625 in) thick AA2219-T87. The optimal process parameter set (traversing speed and rotational speed) was determined in a previous proprietary study completed at Marshall Space Flight Center (MSFC) in Huntsville, Alabama. The weld specimens were prepared from as-purchased, 19.05 mm (0.75 in) thick aluminum plate. Once received, the top and bottom plate surfaces were machined to remove 1.59 mm from each side, resulting in a 15.875 mm (0.625 in) thick plate. The plate was then sheared into 762 mm by 152.4 mm weld coupons. The plate orientation was such that the 762 mm length aligned with the longitudinal (rolling) direction and the 152.4 mm side aligned transverse to the rolling direction. Two 762 mm by 152.4 mm by 15.875 mm weld coupons were used to create a single weld panel by use of butt-weld configuration.

### 4.2.1. Residual Stresses

Residual stress spot measurements were conducted on the SR-FSW plate by use of an iXRD Residual Stress Analyzer from Proto Manufacturing. The measurements were conducted using a penetration depth and working volume of 94.16  $\mu\text{m}$  and 0.296  $\text{mm}^3$ , respectively. Measurements were made on the crown side of the weld. A schematic indicating the locations where the residual stress spot values were measured is provided in Figure 4.1. Note, residual stresses in the longitudinal (parallel with the weld) and transverse (perpendicular with the weld) directions were measured.

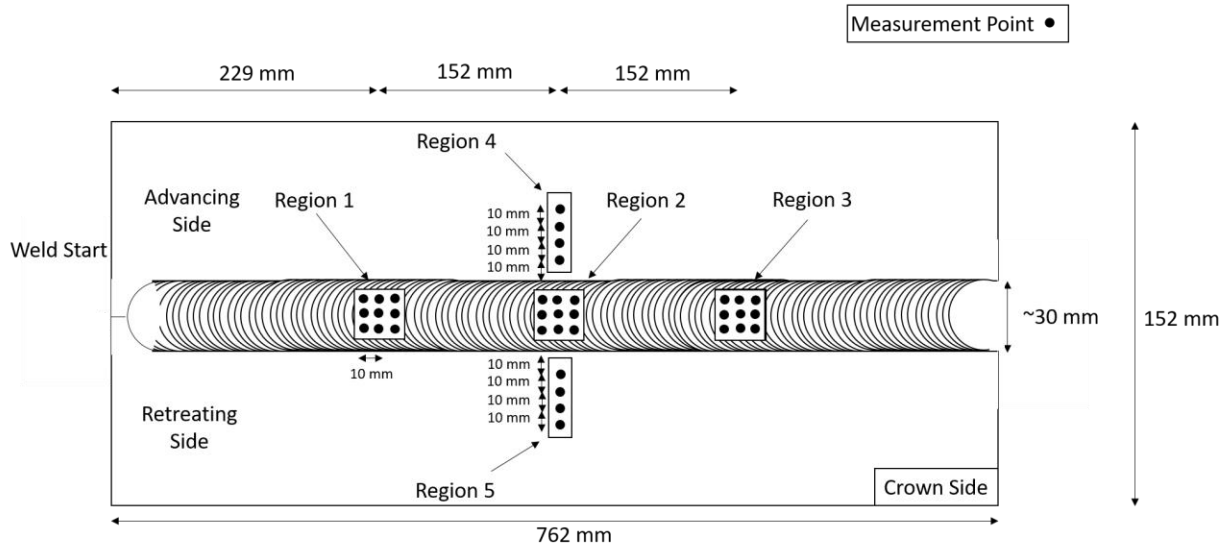


*Figure 4.1.* Schematic indicating locations of residual stress spot measurements.

Additionally, longitudinal residual stresses were measured along a 100 mm path running perpendicular to the weld. The residual stress measurements were conducted from the crown side of the plate and were located 381 mm from the left hand edge of the plate (as shown in Figure 4.1). The line scan starts in the advancing side of the weld, approximately 50 mm from the weld centerline, and passes perpendicular to the weld direction to approximately 50 mm into the retreating side of the weld. As before, the penetration depth was set to 94.16  $\mu\text{m}$  and the working volume was 0.296 mm<sup>3</sup>.

Spot-location longitudinal residual stress measurements of the SR-FSW panel made by use of optimal process parameters are presented in Figure 4.2. The data indicates that the longitudinal residual stresses measured at the advancing side of the weld are relatively consistent as a function of weld progression. Further, longitudinal residual stress values measured at the advancing side are nearly always larger than those measured on the retreating side, regardless of weld progression. One will note that the longitudinal residual stresses measured on the retreating

side of the weld increase in magnitude, from near zero at 229 mm weld progression, to approximately 100 MPa at 533 mm weld progression.

Advancing Side								
Longitudinal			Region 4			Region 5		
Region 1			Region 2			Region 3		
117.2	113.2	114.5	123.5	113.6	119.2	119.2	120.9	121.1
103	93	97	98.1	96.4	96.6	94.3	107.1	103.6
5.9	12.1	13.8	36.5	50.7	46.5	109.3	99.6	97
			Region 4			Region 5		
			-44.5	-68.3	-45.9	-51.5	-75.3	8.9
			38.9			-42.7		
Retreating Side								
Direction of Weld Travel →								

*Figure 4.2. Residual stress values in the longitudinal direction measured at spot locations indicated in Figure 4.1 (crown side of plate). Magnitudes are MPa.*

Spot-location transverse residual stress measurements of the SR-FSW panel made by use of optimal process parameter set are presented in Figure 4.3. While all spot longitudinal residual stress data collected in the weld exhibited tensile values, the transverse residual stress spot measurements exhibited compressive values. Furthermore, the compressive transverse residual stress values are on the order of one-third the magnitude of the tensile longitudinal values.

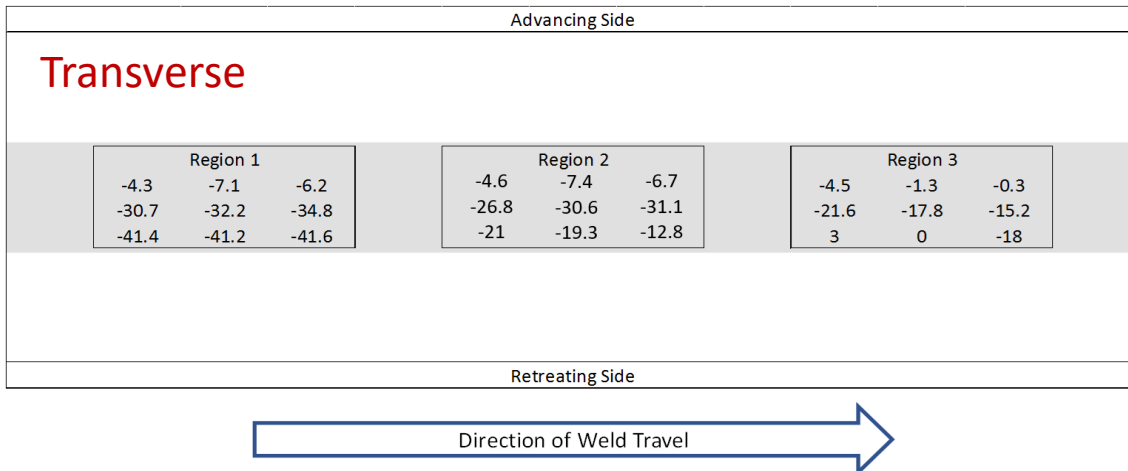


*Figure 4.3.* Residual stress values in the transverse direction measured at spot locations indicated in Figure 4.1 (crown side of plate). Magnitudes are MPa.

Longitudinal residual stresses were measured at the center of the weld panel along a 100 mm long path perpendicular to the axis of the weld. The line-scan longitudinal residual stress data is provided in Figure 4.4 with error bars representing  $\pm 1$  standard deviation of the measurements. The longitudinal residual stress line-scan exhibits the expected shape found in FSW measurements with a maximum magnitude of 117 MPa in the stir zone, a minimum value of -94 MPa in the retreating-side TMAZ, and a consistent advancing-side residual stress value of approximately -60 MPa.

The residual stress measurements presented in this section provide insight later in the work about differences in material properties observed in the SR-FSW material.

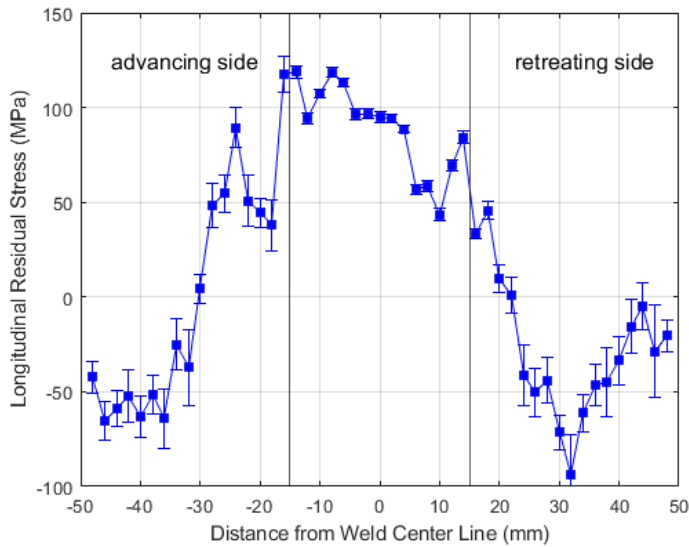


*Figure 4.4. Line scan of longitudinal residual stresses.*

#### 4.2.2. Grain Morphology

Grain sizes in respective locations of the weld were measured per ASTM standard E112.

Samples were hot mounted in phenolic resin and subsequently ground using successively finer SiC paper (240 grit, 600 grit, 800 grit, followed by 1200 grit SiC). The samples were then polished using 1  $\mu\text{m}$  diamond suspension and 0.4  $\mu\text{m}$  colloidal silica suspension, followed by chemical etching in Keller's reagent for 15 seconds.

Figure 4.5 shows optical micrographs of the stir zone, TMAZ, HAZ, and base material. The primary subimages are all taken at the same magnification. The micrographs were obtained from the cross section of the retreating side of the weld. Grain sizes are listed for each zone in Table 3. The designations S and T in Table 4.1 indicate the direction that the measurements were taken on the longitudinal plane, respectively. As expected, fine equiaxed grains were observed in the stir zone due to the large plastic deformation and dynamic recrystallization effects of the SR-FSW process. These grains are on the order of 8 to 12 microns and gradually increase in size between the advancing and retreating side of the stir zone. Elongated grains were observed in the

HAZ, and base material on the order of 2:1. The TMAZ exhibited elongated grains on the order of 4:1.

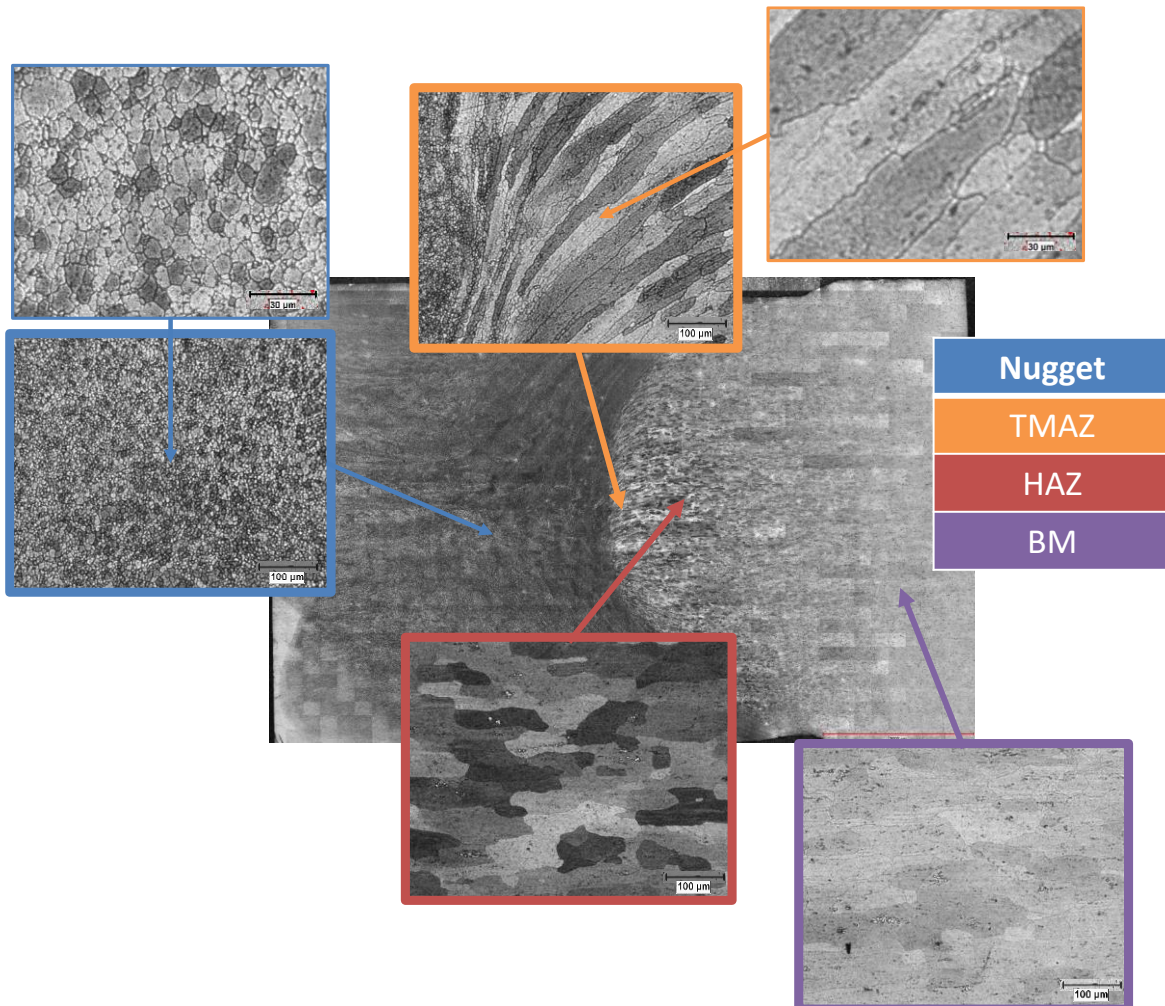


*Figure 4.5. Micrographs of grain size in respective locations of SR-FSW.*

*Table 4.1. Grain size measurements on the longitudinal plane for AA2219 aluminum SR-FSW by use of nominal process parameters. All units are in microns.*

	Base Material		HAZ		TMAZ		Nugget
	S	T	S	T	S	T	*equiaxed grains
Grain Size	26	49	28	66	59	90	8-12
Standard Deviation	2.3	14.1	1.6	6.9	7.9	5.6	0.3-0.5

#### 4.2.3. Microhardness

Transverse cross-sections of the SR-FSW were removed from the weld panel for microhardness mapping. Two specimens were required in order to characterize the weld TMAZ, weld HAZ and base material on both sides of the weld. Samples were cold mounted in epoxy resin and subsequently ground, polished, and chemical etching following the same methods described in Section 4.2.2 for grain size measurement.

Microhardness measurements were performed by use of a Clemex CMT microindenter. A single indent force was used for all regions of the sample (base material, stir zone, TMAZ). Once the indent force and subsequent indent size was determined based upon indent measurements taken from the softest region for the mapping area, indent spacing was set at 2.5 times the optimal indent size. Ultimately, an array of (85 by 55) indents were created having 250  $\mu\text{m}$  spacing to map an area of 283.5  $\text{mm}^2$  for each sample. The data was then stitched together electronically to create a single microhardness map.

Figure 4.6 provides the microhardness map of a cross section of a SR-FSW created by use of optimal process parameters. The low hardness observed in the stir zone of the weld is likely caused by a lack of strengthening precipitates in existence inside the weld. Given that temperatures as high as 500C would likely have been reached inside the stir zone of the weld, the primary strengthening phases ( $\theta'$  and GP zones) would have been depleted, leaving only large  $\theta$  phase agglomerations in existence. As you move from the stir zone to the TMAZ, HAZ, and into the base material, the measured hardness increases. This increase in hardness correlates with the decrease in the magnitude of temperature experienced by the material during welding.

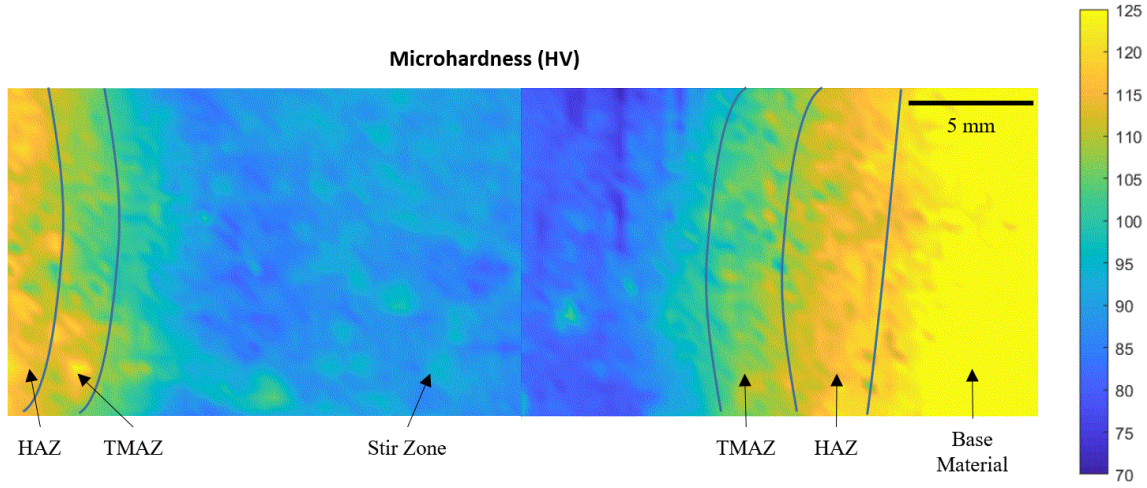


*Figure 4.6. Microhardness map of AA2219-T87 SR-FSW built using the optimum process parameter set.*

#### 4.3. Fatigue Crack Growth and $K_{IC}$ Testing

All constant amplitude FCG tests were performed per ASTM E647 using a load ratio ( $R$ ) of  $R=0.1$  and frequency of  $f=10$  Hz. All samples were precracked to  $a/W=26.3$ . The load amplitudes used for each test are shown in Table 4.2.

*Table 4.2. Load amplitudes used for FCG tests.*

Sample ID	Load Amplitude (N)
Base Material 1	3240
Base Material 2 and 3	1935
All stir zone and TMAZ samples	2700

Fracture toughness ( $K_{IC}$ ) tests were performed in accordance with ASTM E399. The fatigue precracking procedures for the  $K_{IC}$  tests grew a sharp initial crack of length  $a=0.50W$  and final  $\Delta K$  values ranging from 13 to 17 MPa $\sqrt{m}$ . All testing was conducted at room temperature using a 20 kN closed-loop servohydraulic testing machine outfitted with commercially available control software.

Crack length in the C(T) specimens was monitored with a crack mouth opening displacement (CMOD) gage attached to attachment points machined on the front edge of the specimen. The fatigue crack growth rate was calculated using the central finite difference (CFD) method.

#### 4.3.1. Specimens

ASTM E647 details the recommended specimen geometry to ensure the generation of test data that can be repeated by other laboratories and in literature. An overview of the standard geometry is detailed in CHAPTER 2. The specimens used for testing were standard 2 in C(T) samples and were compliant with E647. The thickness  $B$  is 12.7 mm (0.5 in). The sample drawing is shown in Figure 4.7.

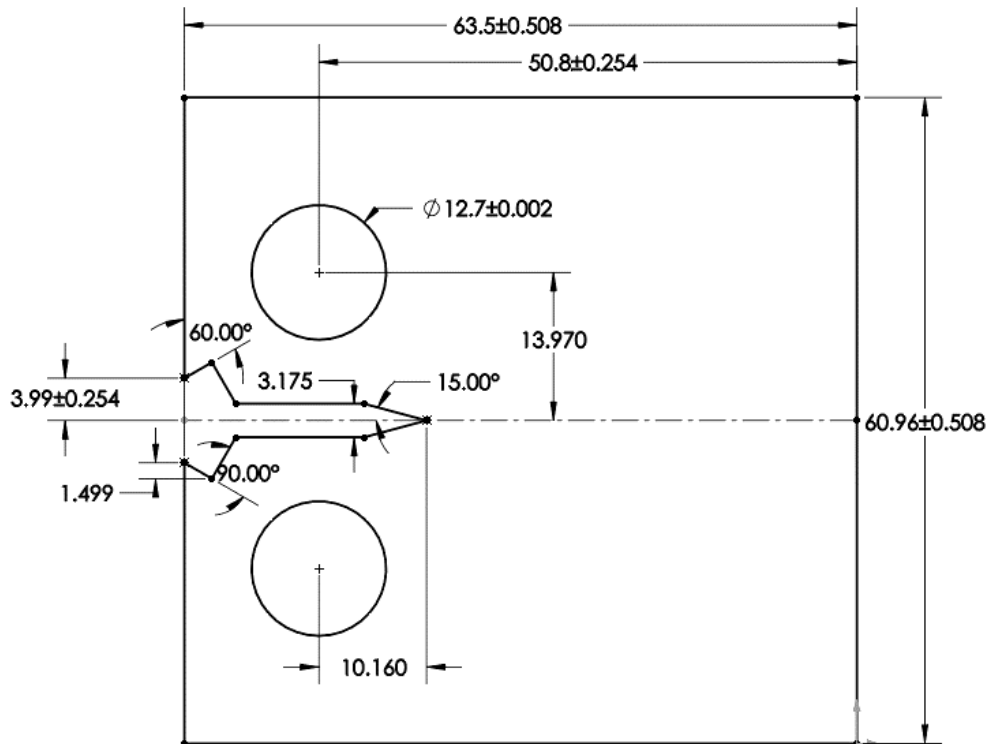


*Figure 4.7. Final FCG and  $K_{IC}$  sample geometry. All units are in millimeters. Thickness  $B$  is 12.7 millimeters.*

#### 4.3.2. FCG Test Matrices

The C(T) samples were machined with the intent of initiating sharp initial cracks in the base material, stir zone, and TMAZ of AA2219 SR-FSW panels. The stir zone and TMAZ locations were approximated using the microhardness data taken from Section 4.2.3. Figure 4.8 provides images of the etched C(T) specimens demonstrating the alignment of the crack within the stir zone (a) and TMAZ (b). For these samples, the crack ran in the longitudinal direction of the welded plates, and the axial force was exerted in the transverse direction, designated as T-L. Base material samples were machined from a separate wrought plate sourced from the same material lot, also in the T-L orientation.

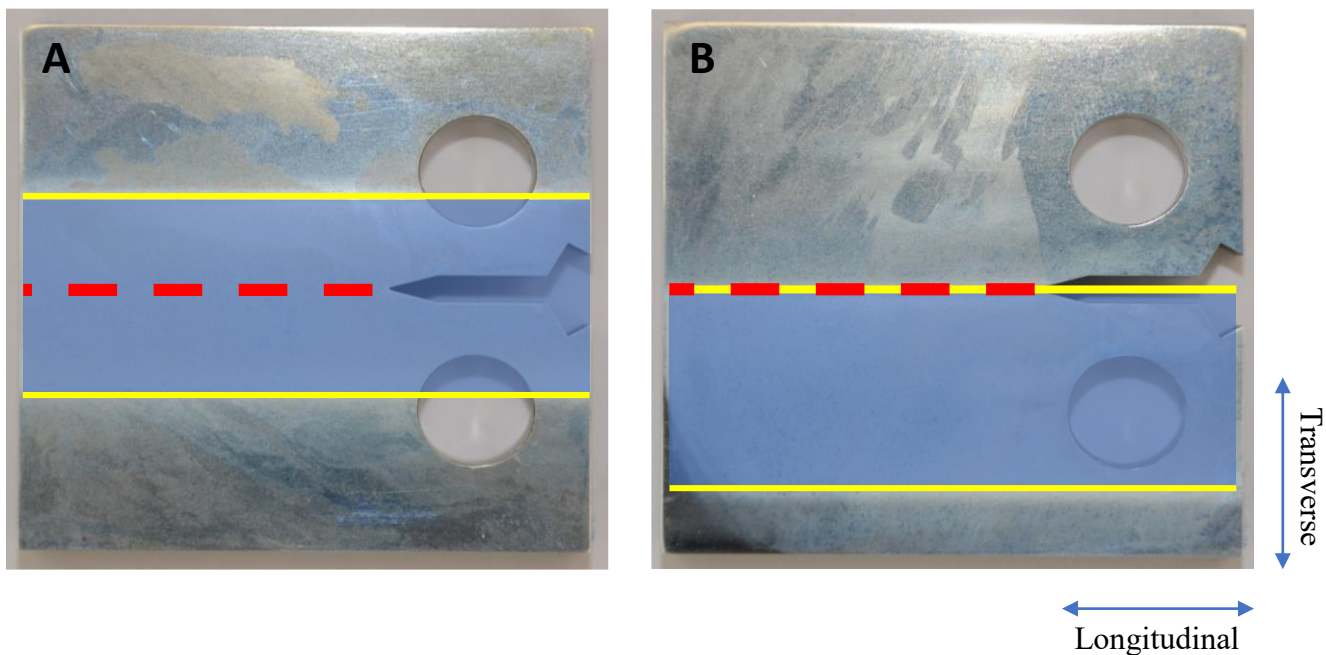


Figure 4.8. Images of C(T) specimens showing where the stir zone (blue) and TMAZ (yellow) exist relative to the crack (red) intended path. Image (a) and image (b) represent stir zone and TMAZ samples, respectively.

#### 4.3.3. FCG Test Results and Conclusions

FCG data for the base material, TMAZ, and stir zone are presented in

Figure 4.9.

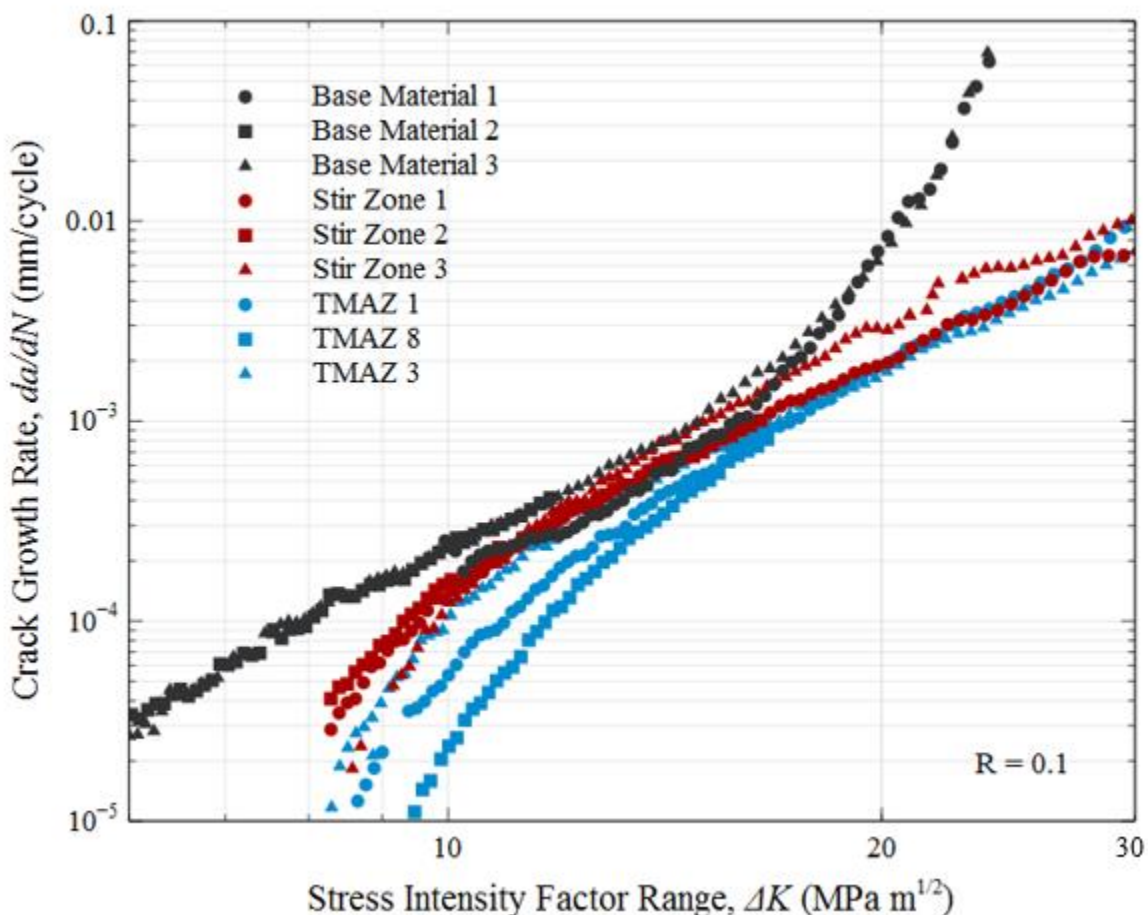


Figure 4.9. Fatigue crack growth data for base material, TMAZ, and stir zone samples.

It is observed that the TMAZ and stir zone resist crack growth better than the base material in the lower  $\Delta K$  portion of the curve. Generally, a change in fatigue behavior can be attributed to a combination of residual stress and crack closure effects in mechanically processed materials (Suresh, 1998). Given that the cracks propagate in the longitudinal orientation where residual stresses measured in Section 4.2.1 are an order of magnitude larger than those in the

transverse orientation, the effect of residual stresses is likely minimal. Crack closure measurements taken from the data below indicate an increasing effect of crack closure in the base material, stir zone, and TMAZ data, respectively for  $\Delta K$  below 10 MPa $\sqrt{m}$ . These measurements followed ASTM E647's recommended practice for crack opening force determination using the compliance offset method. A total of nine measurements were made for each sample. Three measurements were made in each of the following  $\Delta K$  ranges: 0 to 10 MPa $\sqrt{m}$ , 10 to 20 MPa $\sqrt{m}$ , and 20 to 30 MPa $\sqrt{m}$ . Average normalized crack opening loads for each location and  $\Delta K$  range are presented in Table 4.3.

Table 4.3. *Average crack opening load as a function of weld location and  $\Delta K$ .*

Location	Normalized Crack Opening Load		
	$\Delta K$ between 0 to 10	10 to 20	20 to 30
Base Material	0.30	0.32	0.28
Stir Zone	0.54	0.30	0.33
TMAZ	0.64	0.35	0.33

These results are as expected as plasticity induced crack closure (PICC) can influence the crack growth behavior of highly ductile materials (Suresh, 1998). As previously postulated from correlations to isothermal hardness results, the material in the stir zone experiences temperatures at or near the eutectic as a result of the welding process. This thermal exposure depletes the strengthening precipitates, resulting in a weld material of high ductility and low strength. This combination creates an opportunity for crack growth rates to slow due to PICC. In addition to PICC, fracture surfaces of the TMAZ were rougher showing more fretting than the other samples, indicating roughness induced crack closure (RICC) also likely contributed to the deceleration of growth in the TMAZ. An image of the representative fracture surfaces is shown in Appendix Figures A.8 to A.10.

A difference in crack growth rate of the welded and base material samples is also observed in the higher  $\Delta K$  portion of the curve. The base material samples show evidence of Region III crack growth at a  $\Delta K$  of 20 MPa $\sqrt{m}$ . This is not surprising given the expected  $K_{IC}$  for the material is near 30 MPa $\sqrt{m}$  (Gallagher, 1983). The stir zone and TMAZ samples, however, continue with the same slope observed in Region II. This is perhaps due to a breakdown of  $K$  similitude as more plasticity occurs in the sample.

#### 4.3.4. $K_{IC}$ Test Results and Conclusions

Plane-strain fracture toughness  $K_{IC}$  tests were completed for the base material, stir zone and TMAZ. The load-displacement plots are given in Appendix Figures A.11 to A.13. The stir zone and TMAZ samples were machined from the welded plate at the relative locations described in Section 4.3.2. Base material samples were cut from the same lot of material.  $K_{IC}$  results for all samples are provided in Table 4.4.

Table 4.4.  $K_{IC}$  values for locations of SR-FSW. \* indicates invalid test per ASTM E399.

Specimen Location	$K_{IC}$ (MPa $\sqrt{m}$ )	Pmax/Pq
Base Material 1	29.9	1.09
Base Material 2	29.05	1.16*
Base Material 3	29.14	1.15*
Base Material 4	30.0	1.13*
Base Material 5	30.3	1.16*
Stir Zone	28.1	1.69*
TMAZ	27.5	1.55*

Four of the five fracture toughness tests performed in the base material were invalid per ASTM 399. The results (slightly) exceed the  $P_q/P_{max}$  limit of 1.10. Even so, the  $K_{IC}$  values determined in this study compare well with those found in literature for AA2219 (Gallagher, 1983). Furthermore, the trend exhibited between the base material and stir zone/TMAZ values matches what one would expect given the relative decrease in strength and increase in ductility between the base material, TMAZ, and stir zone. Additionally, the remaining ligament requirement given in Equation 2.17 is met for samples of all three spatial zones.

The  $P_q/P_{max}$  validity requirements of E399 were also not met for the stir zone and TMAZ sample results. Given that the base material results were determined to still be of value although not in accordance to E399, the welded samples are considered to be acceptable at this time.

#### 4.4. Model Implementation

This work implements a model which helps elucidate and quantify the relative contributions of strengthening mechanisms to the ultimate tensile strength of friction stir welded AA2219. The model is based upon the assumptions presented in CHAPTER 2 where SR-FSW AA2219 is strengthened by the following mechanisms: solid solution strengthening, grain boundary strengthening, grain size strengthening, grain orientation strengthening, and precipitation strengthening. The model follows the functional form,

$$\sigma_{UTS\ total} = \sigma_{UTS\ solid\ solution} + \sigma_{UTS\ grain\ size} + \sigma_{UTS\ grain\ orientation} + \sigma_{UTS\ precipitate}. \quad (4.1)$$

This equation may be simplified to the following form based on the discussion in CHAPTER 2 for grain orientation strengthening,

$$\sigma_{UTS\ total} = \sigma_{UTS\ solid\ solution} + \sigma_{UTS\ grain\ size} \pm 10\% \sigma_{UTS\ solid\ solution} + \sigma_{UTS\ precipitate}. \quad (4.2)$$

Furthering the discussion in Section 3.4 about the effect of thermal history on solution hardening, it is expected that temperatures on the order of 500°C are experienced inside the stir zone of the weld, causing overaging of the material. Temperatures this high are unlikely in the base material (BM), thermomechanical affected zone (TMAZ), and heat affected zone (HAZ) of the weld. In this case, there would be a mix of metastable and stable phases, but no GP zones in these locations. Thus, this work estimates that the contribution to the UTS would be roughly

$\sigma_{UTS\ solid\ solution}=300$  MPa in the stir zone and  $\sigma_{UTS\ solid\ solution}=250$  MPa in all other regions per the results presented in Section 3.4.

The only unknown in Equation ((4.2)) is the contribution to strength from precipitates; therefore, it may be rearranged to

$$\sigma_{UTS \text{ precipitate}} = \sigma_{UTS \text{ total}} - (\sigma_{UTS \text{ solid solution}} + \sigma_{UTS \text{ grain size}} \pm 10\% \sigma_{UTS \text{ solid solution}}). \quad (4.3)$$

Equation (4.3) has been implemented into MATLAB and applied to several SR-FSW process parameter sets. The program begins by binning each weld zone based off of the change in microhardness results and assigning each region a  $\sigma_{UTS \text{ solid solution}}$  and  $\sigma_{UTS \text{ grain size}}$  value. The  $\sigma_{UTS \text{ solid solution}}$  values for the stir zone and TMAZ/HAZ of the weld are 300 MPa and 250 MPa, respectively. The contribution to UTS from grain size follows the Hall-Petch relationship and is based on the grain size measurement results provided in Section 4.2.2. Note, the gradient observed in grain size within the stir zone is accounted for by separating this region into multiple bins.

The process parameters to be studied are highlighted in purple in Figure 4.10. Specifically, there are four process parameter sets surrounding the optimum set studied here shown as green “X”. Each set produces different microhardness results spatially in the weld. The traversing and rotational speeds have been normalized to protect proprietary data from the company who supplied the welds.

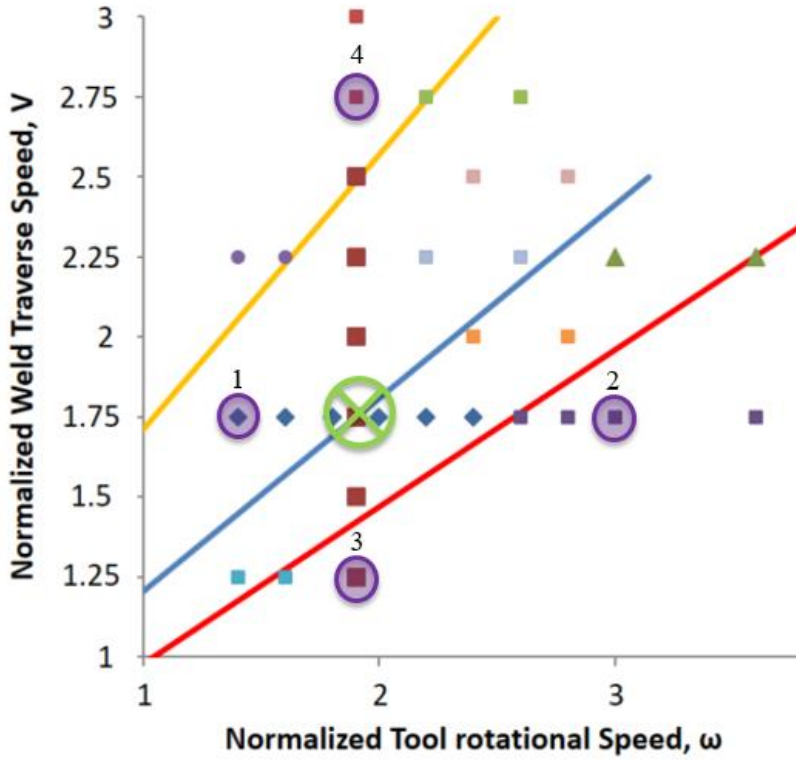


*Figure 4.10.* Process parameter sets to be studied circled in purple. The optimum set is indicated by the green cross.

First, the model is applied to process parameter set #1 which is a nominal weld traversing speed, low tool rotational speed set (1.4, 1.75). The UTS estimated from measured microhardness is presented in Figure 4.11(a), a micrograph of the cross section of the weld is presented in Figure 4.11(b), the predicted contribution to UTS from a combination of grain size and solid solution strengthening is presented in Figure 4.11(c), and the predicted contribution to UTS from precipitates is presented in Figure 4.11(d).

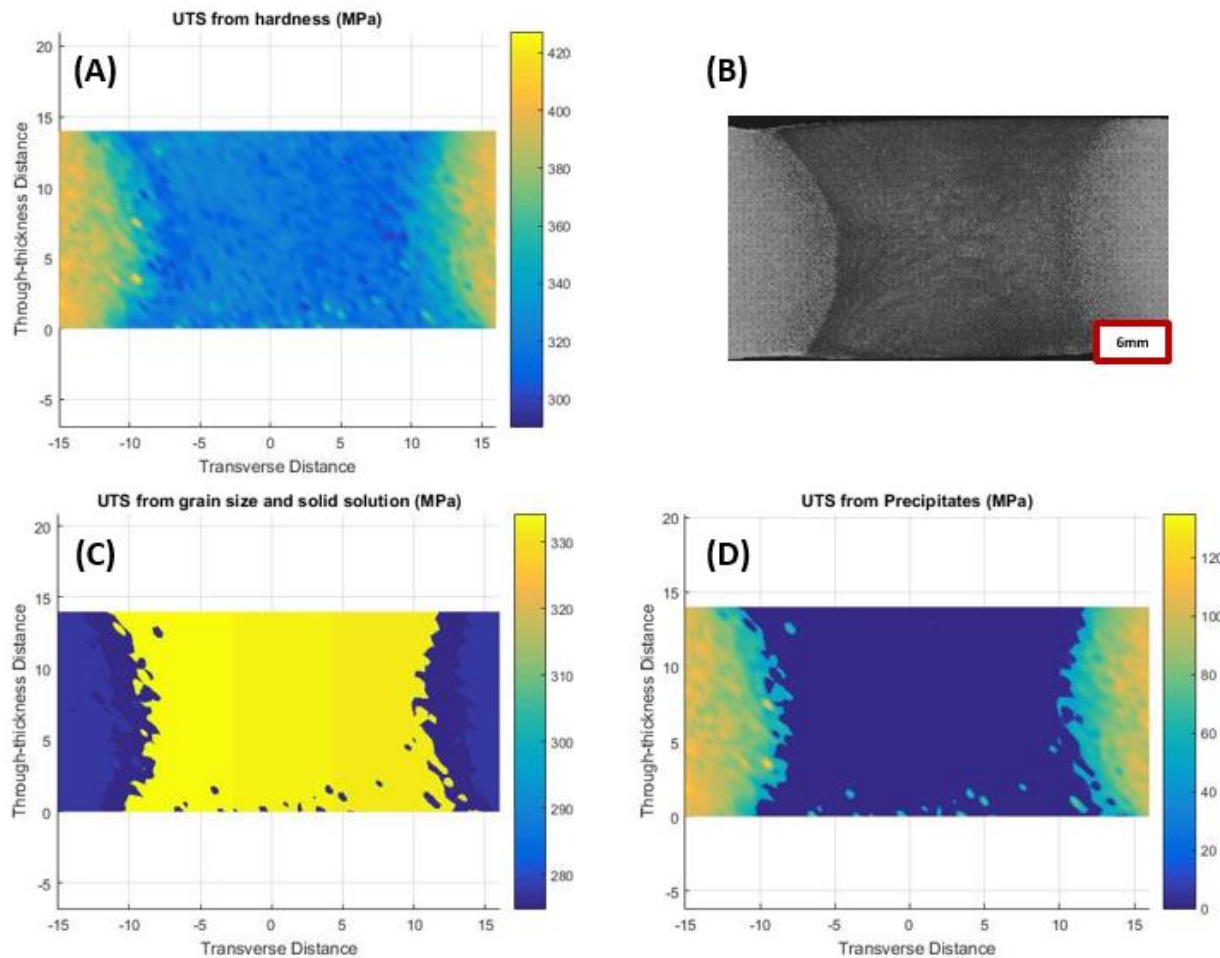


*Figure 4.11. Process parameter set #1. Nominal traversing speed, low rotational speed (1.4, 1.75).*

The results of the model clearly indicate that there is a difference in the contribution to strength from precipitates in the various spatial zones of the weld. There are no effects of precipitation hardening in the stir zone of the weld while there is a contribution of approximately 60 MPa to the UTS in the TMAZ. Likely, the primary strengthening precipitates were depleted in the stir zone due to high temperatures, and relatively lower temperatures retained the strengthening phases in the TMAZ. Additionally, the weld produced using this parameter set will be low strength and very ductile.

Next, the model is applied to process parameter set #2 where the SR-FSW is created using the nominal traversing speed and a high rotational speed. The UTS estimated from measured microhardness is presented in Figure 4.12(a), a micrograph of the cross section of the weld is presented in Figure 4.12(b), the predicted contribution to UTS from grain size and solid solution strengthening is presented in Figure 4.12(c), and the predicted contribution to UTS from precipitates is presented in Figure 4.12(d).

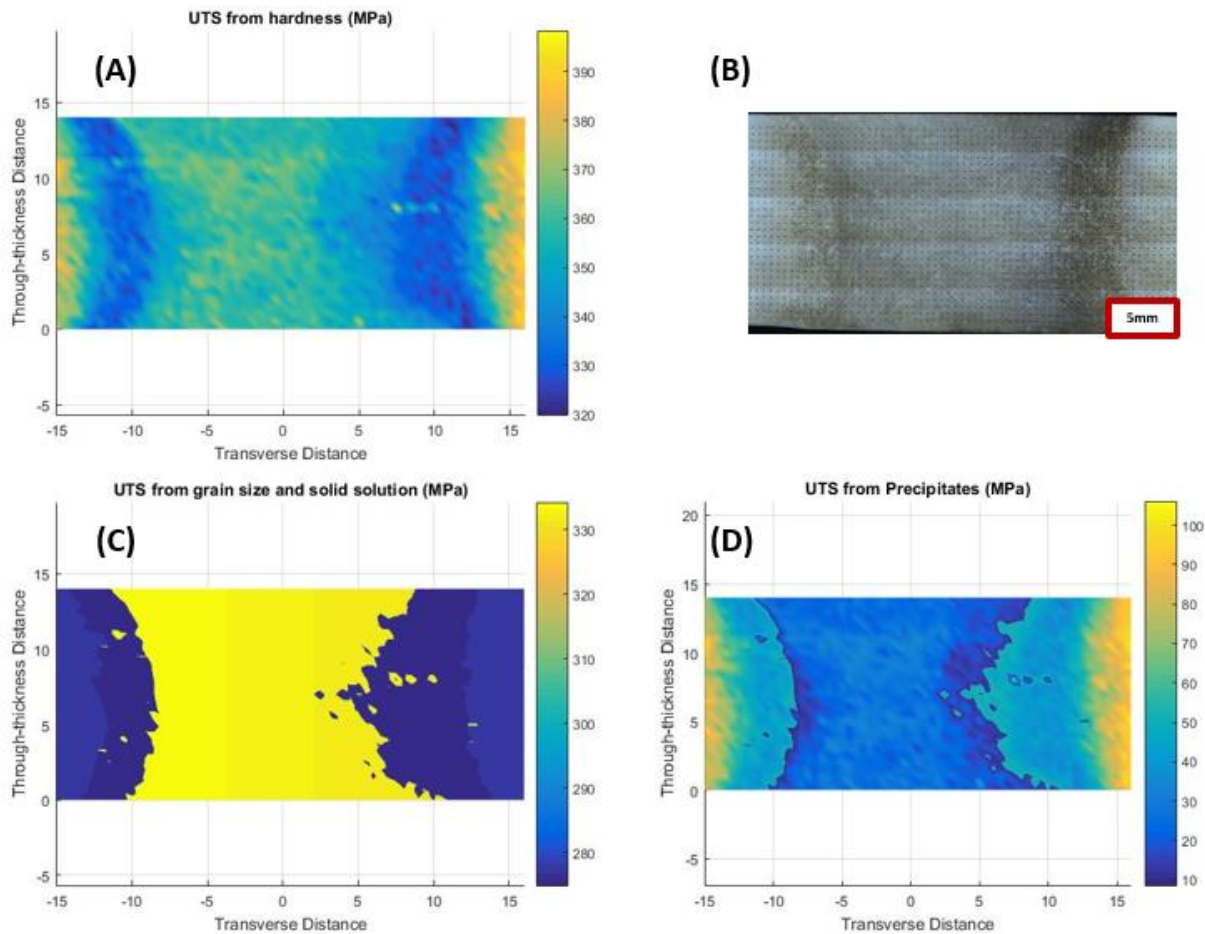


Figure 4.12. Process parameter set #2. Nominal traversing speed, high rotational speed (3,1.75).

The spatial plot shown in Figure 4.12(d) indicates that there are strengthening precipitates in both the stir zone and TMAZ of the weld. The stir zone is predicted to have a contribution of

roughly 40 MPa, and the TMAZ experiences a slightly higher contribution of 55 MPa. The weld produced using this process parameter set will likely be relatively strong and ductile.

The spatial plots for the remaining process parameter sets can be found in the Appendix Figures A.14 through A.15. However, Table 4.5 shows the predicted precipitate strength contributions for all process parameters studied. In its current state, this model provides a tool to the welding engineers at NASA to better understand the effects of the process parameters on the mechanical properties of their welds. While not yet fully calibrated, the results of the model are reasonable and provide valuable information to its users.

*Table 4.5. Predicted precipitate strengthening contributions for stir zone and TMAZ for five process parameter sets.*

Process Parameter Set	Stir Zone (MPa)	TMAZ (MPa)
#1 (1.4, 1.75)	0	60
#2 (3, 1.75)	40	55
#3 (1.9, 2.75)	25	50
#4 (1.9, 1.25)	0	70

Further, the predictions discussed in this section support the discussion of Section 4.3.3 about the effects of crack closure in the C(T) samples machined in the stir zone and TMAZ of the weld. The relatively low levels of precipitation hardening predicted by the model in the welded material as compared to the base material suggest that the welded material will be more susceptible to PICC than the base material. Additionally, given that the stir zone always indicates lower levels of precipitation strengthening, it likely experiences larger levels of PICC than the TMAZ. This would suggest that the slower crack growth rates in the lower  $\Delta K$  portion of the curve observed in the TMAZ sample can primarily be attributed to RICC in addition to PICC.

## CHAPTER 5 CONCLUSIONS AND FUTURE WORK

### 5.1. Conclusions

The goal of this work was to develop a better understanding of the process parameters used in the self-reacting friction stir welding process by use of data collection, testing, and analysis of AA2219-T87. Specifically the following data were produced: (1) phase transformation kinetics for the virgin material were quantified, (2) residual stresses in the weld were quantified, (3) grain morphology produced by the FSW process was quantified, (4) microhardness was quantified for the base material, weld nugget, and thermo-mechanically affected zone (TMAZ), and heat affected zone (HAZ), (5) the fatigue crack growth rate behavior and fracture toughness values was quantified, and (6) relative amounts of crystalline strengthening mechanisms were postulated spatially as a function of the welding process through a model in MATLAB.

The data produced and analyzed in this work provide NASA's SLS team a more thorough explanation of the impacts of various process parameters on SR-FSW material. It also provides the foundation of a model that can predict the temperature spatially throughout the weld. Ultimately, this work is a step towards increasing the reliability of the SLS rocket through SR-FSW process parameter optimization.

### 5.2. Future Work

While this work has laid a solid framework for the understanding SR-FSW AA2219, more work can be performed. Specific suggestions for future research are as follows:

- Further plane-strain fracture toughness testing of the welded material should be completed to form a statistically significant data set. Work might also be done to account for plasticity effects in the load-displacement curve.
- Additional research may be done on why the growth rate of the welded samples does not show evidence of Region III crack growth.
- The MATLAB model presented in this work may be calibrated using measured precipitate values from the welded material and base material. This may be done by use of TEM (for GP zones) and SEM (for  $\theta'$  and  $\theta$  phases). This would allow the further development of this model such that the heat input for a given set of process parameters may be quantified.
- The MATLAB model presented in this work can be applied to material created using the solid-state additive deposition process to quantify strengthening contributions.

## REFERENCES

- Anderson, T. (2005). *Fracture Mechanics Fundamentals and Applications*.
- Ashby, M. M. (2009). *Engineering Materials and Processes Desk Reference*.
- ASM. (n.d.). *Matweb*. Retrieved from  
<http://asm.matweb.com/search/SpecificMaterial.asp?bassnum=MA2219T62>
- (2013). *ASTM E112-13 Standard Test Methods for Determining Average Grain Size*.
- (2017). *ASTM E399-17 Standard Test Method for Linear-Elastic Plane-Strain Fracture Toughness KIC of Metallic Materials*.
- (2015). *ASTM E647-15e1 Standard Test Method for Measurement of Fatigue Crack Growth Rates*.
- Bannantine, J. C. (1990). *Fundamentals of Metal Fatigue Analysis*.
- Buccio, M. (1993). *ASM Metals Reference Book*.
- Bjorkman, G. C. (2003). *Self-reacting friction stir welding for aluminum alloy circumferential weld application*. Retrieved from  
<https://ntrs.nasa.gov/archive/nasa/casi.ntrs.nasa.gov/20030061190.pdf>
- Broek, D. (1983). *Elementary Engineering Fracture Mechanics*.
- Dieter, G. E. (1986). *Mechanical Metallurgy* (3rd ed.).
- Elangovan, K. B. (2007). Influences of pin profile and roational speed of the tool on the formation of friction stir processing zone in AA2219 AA. *Materials Science and Engineering A*.
- Elber, W. (1970). Fatigue Crack Closure under Cyclic Tension. *Engineering Fracture Mechanics*.
- Gallagher, J. (1983). *Damage Tolerant Design Handbook, MCIC-HB091R* (Vol. Vol 3).
- Hansen, N. (2004). Hall-petch relation and boundary strengthening. *Scripta Materialia*.
- Hutchison, B. (2015). Critical assessment 16: anisotropy in metals. *Materials Science and Technology*.
- Kelly, P. (1972). The effect of particle shape on dispersion hardnening. *Scripta Metallurgica*.
- Papazian. (1982). Calorimetric studies of precipitation and dissolution kinetics in aluminum alloys 2219 and 7075. *Metallurgical Transactions A*.
- Porter, D. E. (1981). *Phase Transformation in Metals and Alloys*.

- Raza, R. A. (2011). Development and Strengthening of 2219 Aluminium Alloy by Mechanical Working and Heat Treatment. *Journal of Applied Sciences*. Retrieved from <https://scialert.net/fulltextmobile/?doi=jas.2011.1857.1861>
- Stephens, R. F. (2001). *Metal Fatigue in Engineering*.
- Suresh, S. (1998). *Fatigue of Materials*.
- Tiyakioglu, M. R.-G. (2015). Hardness–strength relationships in the aluminum alloy 7010. *Materials Science and Engineering A*.
- Vajtai, R. (2013). *Springer Handbook of Nanomaterials*.
- Vickers, J. T. (2016). *NASA Technology Roadmaps, TA 12: Materials, Structures, Mechanical Systems, and Manufacturing*. Retrieved from [https://www.nasa.gov/sites/default/files/atoms/files/2015\\_nasa\\_technology\\_roadmaps\\_ta\\_12\\_materials\\_structures\\_final.pdf](https://www.nasa.gov/sites/default/files/atoms/files/2015_nasa_technology_roadmaps_ta_12_materials_structures_final.pdf)

## APPENDIX



Figure A.1. Micrograph of base material (short orientation) aged at room temperature, 20°C.

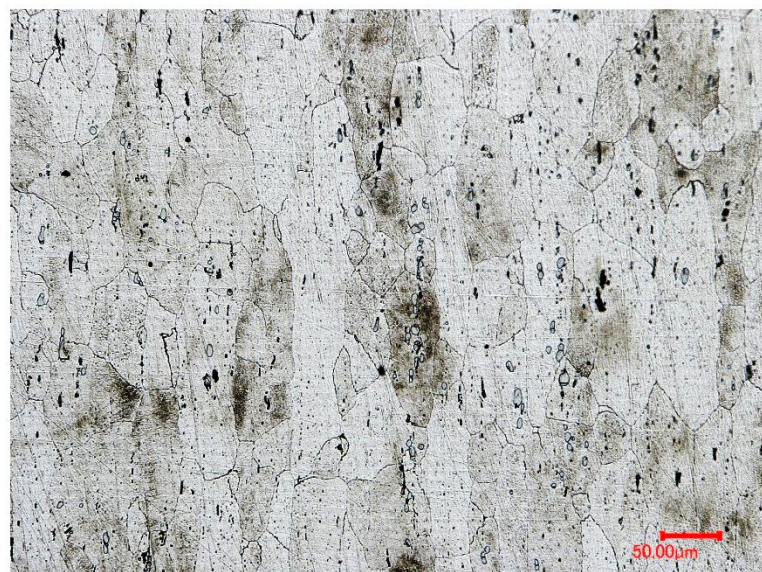
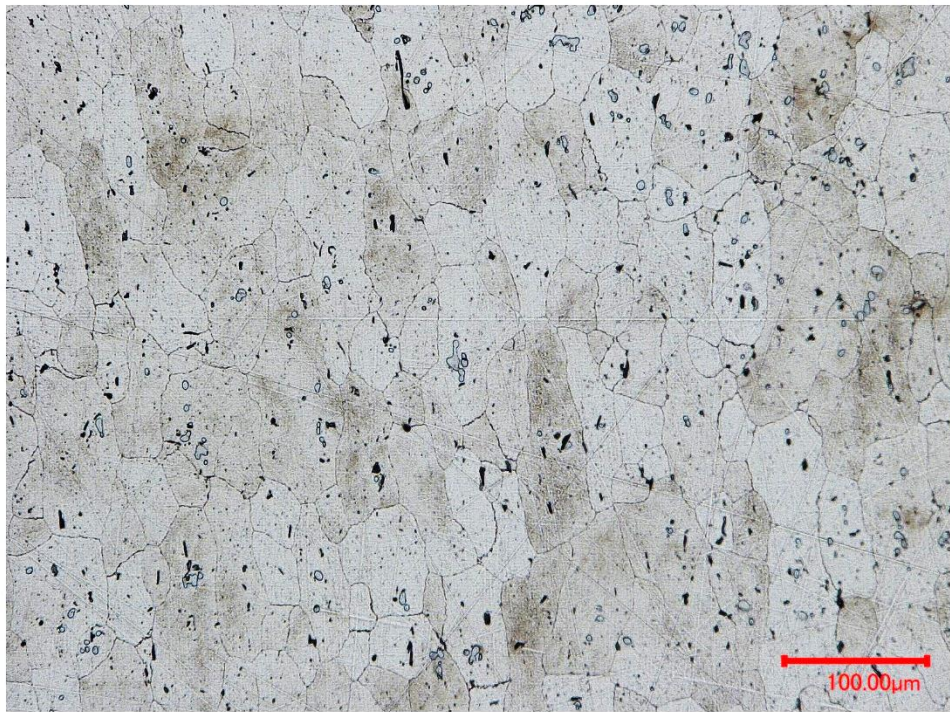


Figure A.2. Micrograph of base material (longitudinal orientation) aged at room temperature, 20°C.



*Figure A.3.* Micrograph of base material (transverse orientation) aged at room temperature, 20°C.



Figure A.4. Micrograph of AA2219 aged at 150°C for 2.8 hours.



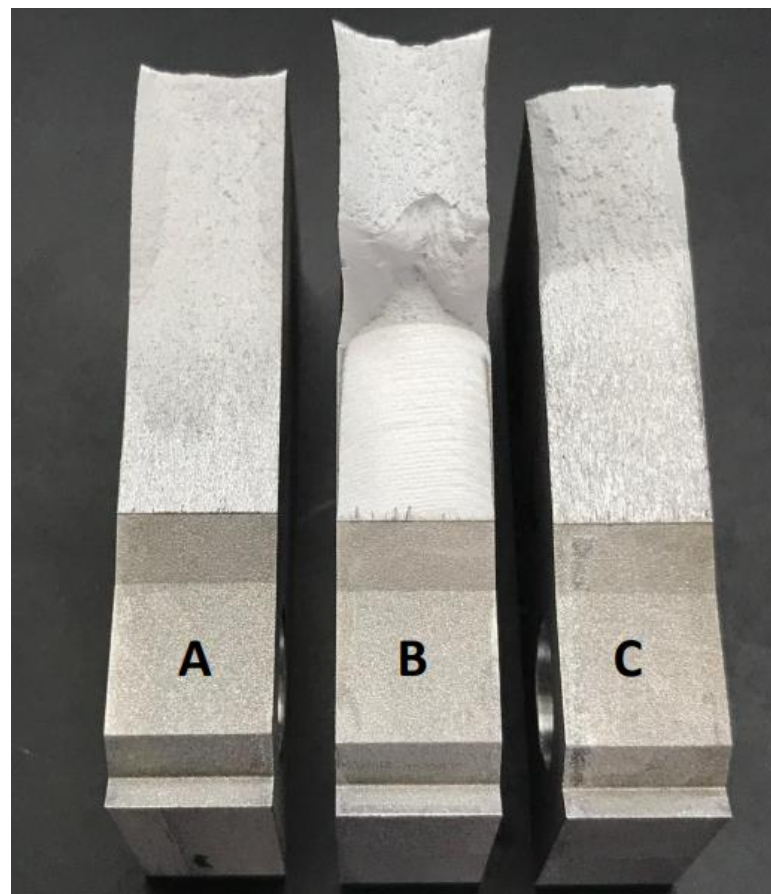
Figure A.5. Micrograph of AA2219 aged at 250°C for 2.8 hours.



Figure A.6. Micrograph of AA2219 aged at 300°C for 2.8 hours.



Figure A.7. Micrograph of AA2219 aged at 425°C for 2.8 hours.



*Figure A.8.* Representative FCG and  $K_{IC}$  fracture surfaces for the base material (A), stir zone (B), and TMAZ (C).

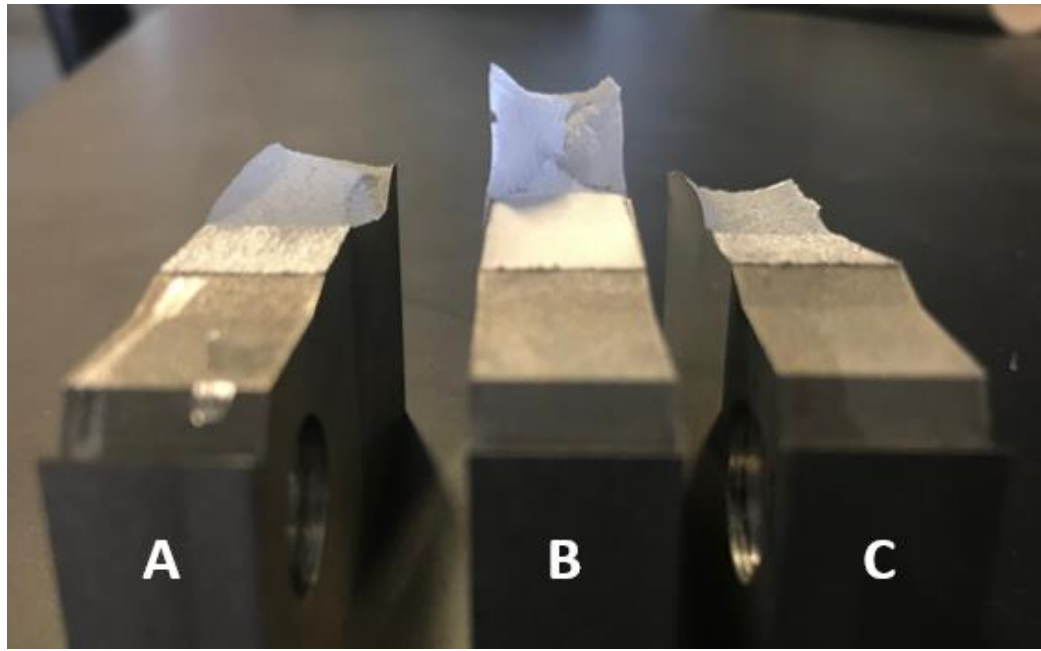


Figure A.9. Representative FCG and  $K_{IC}$  fracture surfaces for the base material (A), stir zone (B), and TMAZ (C).

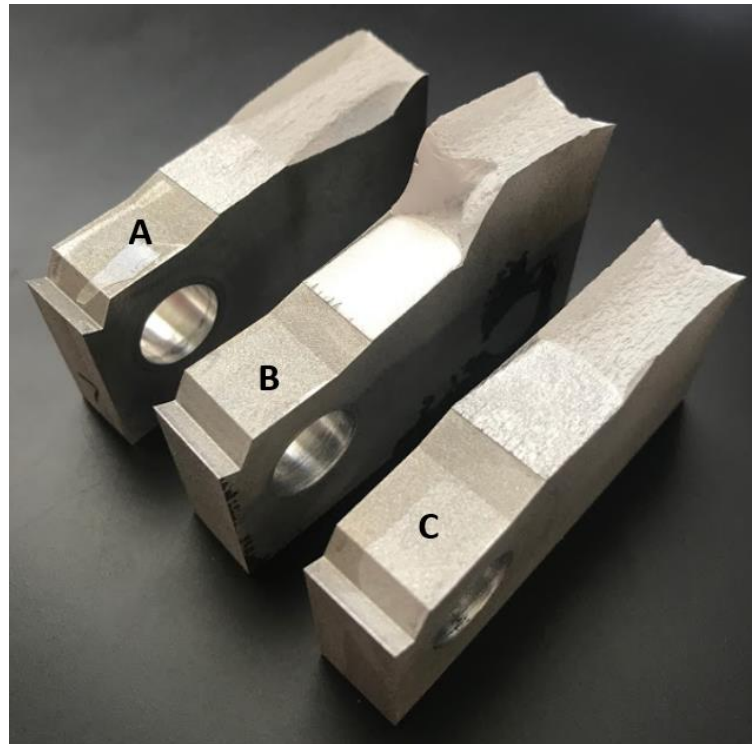


Figure A.10. Representative FCG and  $K_{IC}$  fracture surfaces for the base material (A), stir zone (B), and TMAZ (C).

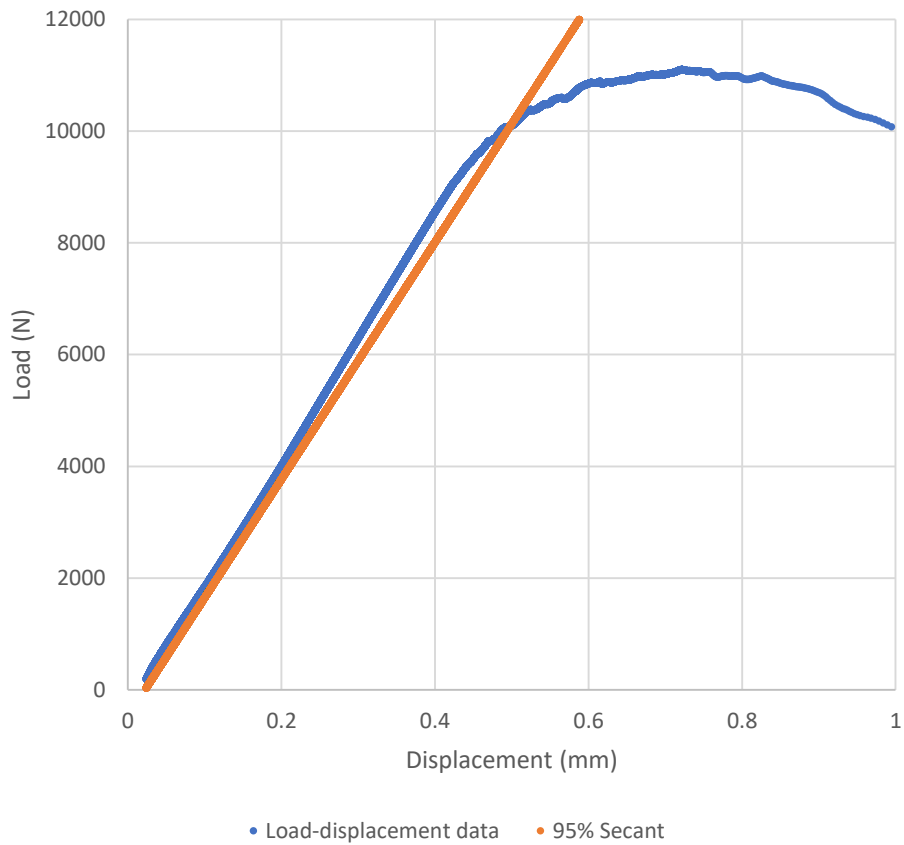


Figure A.11. Representative load-displacement plot for base material K<sub>IC</sub> sample.

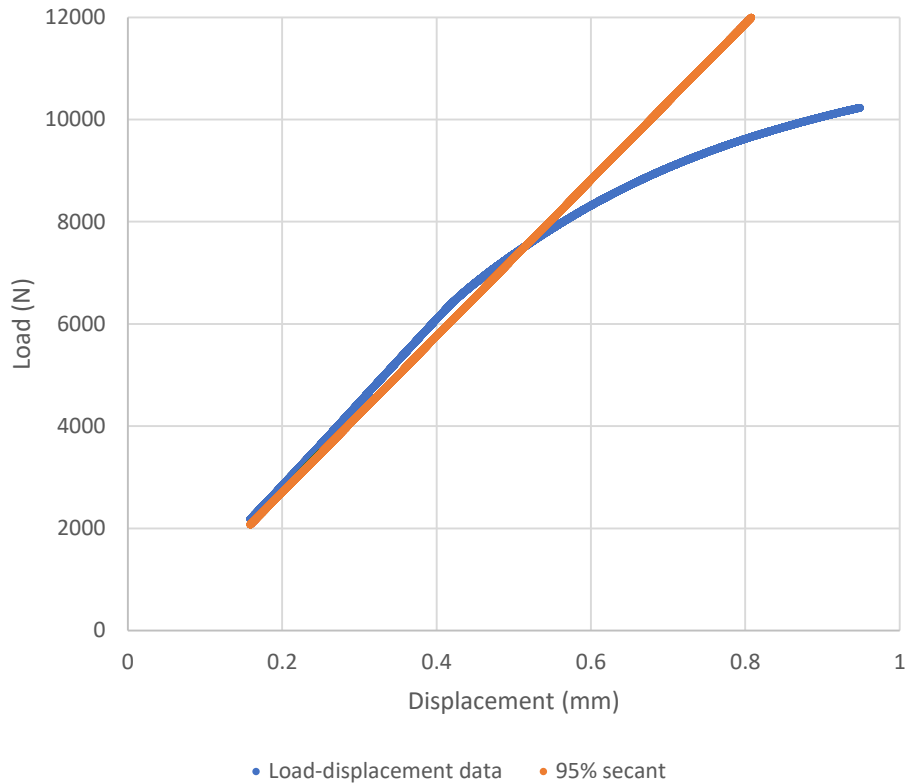


Figure A.12. Load-displacement plot for stir zone K<sub>IC</sub> sample.

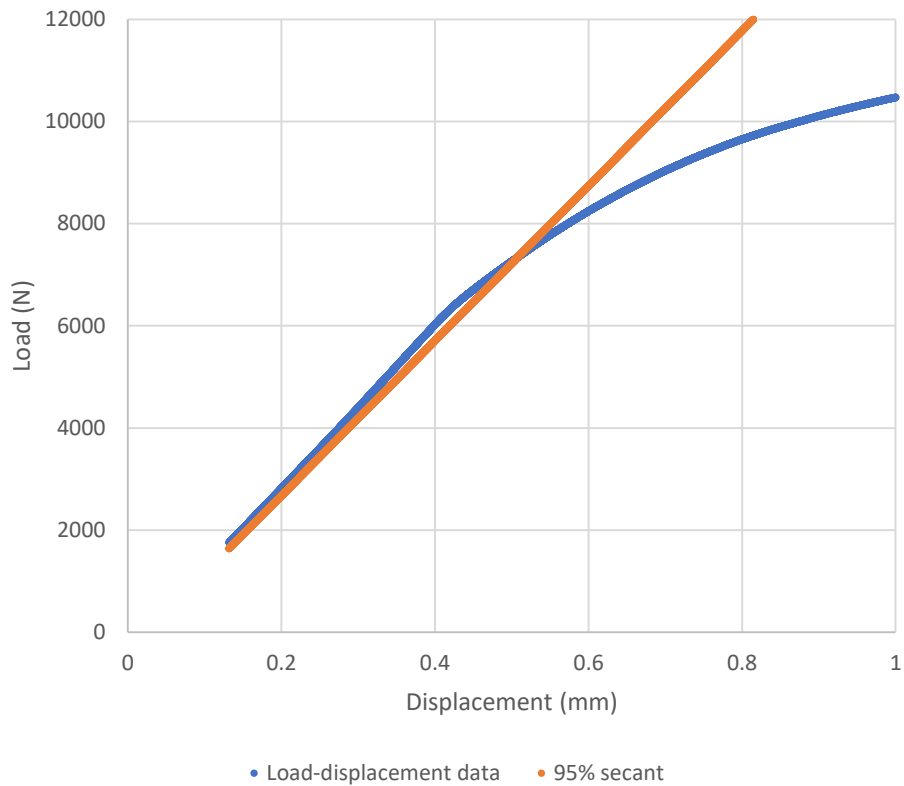
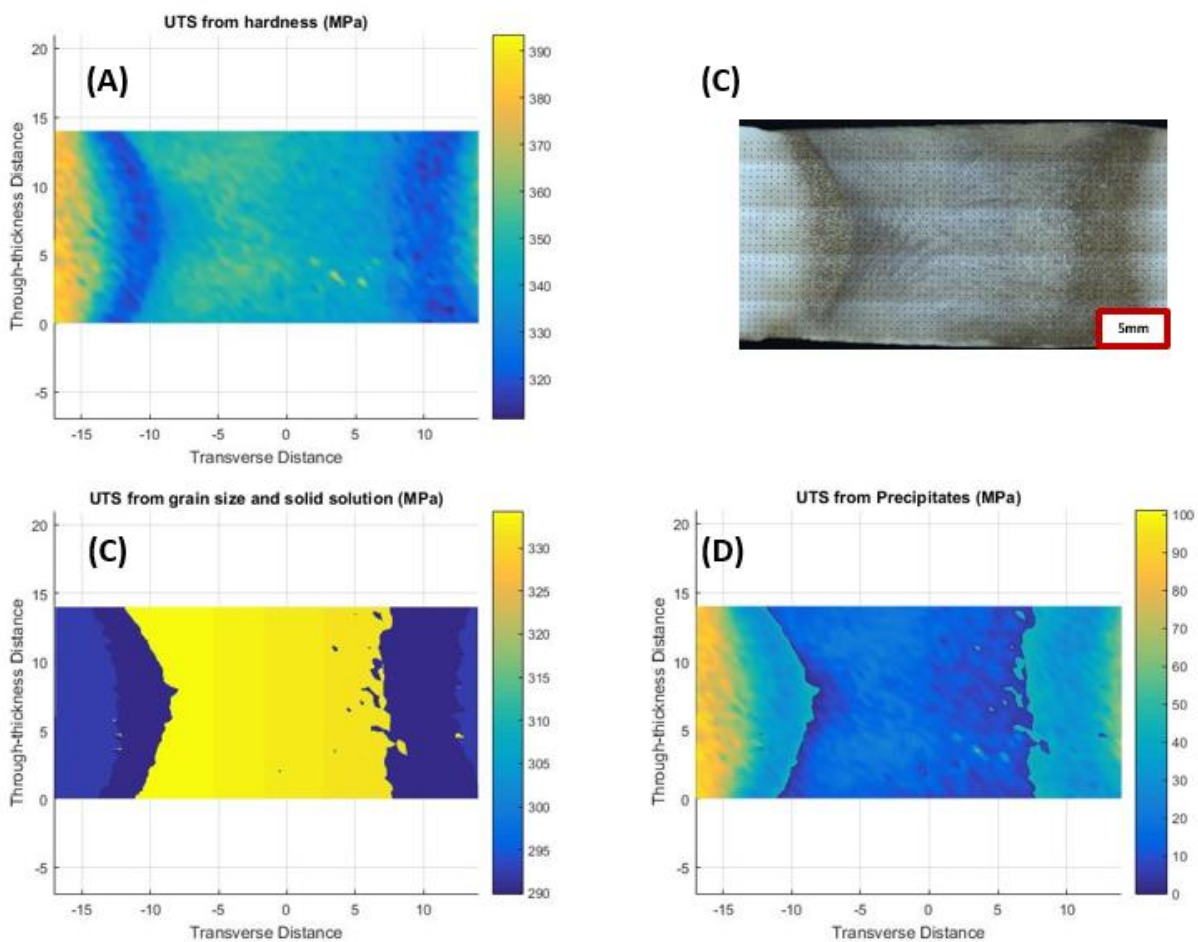
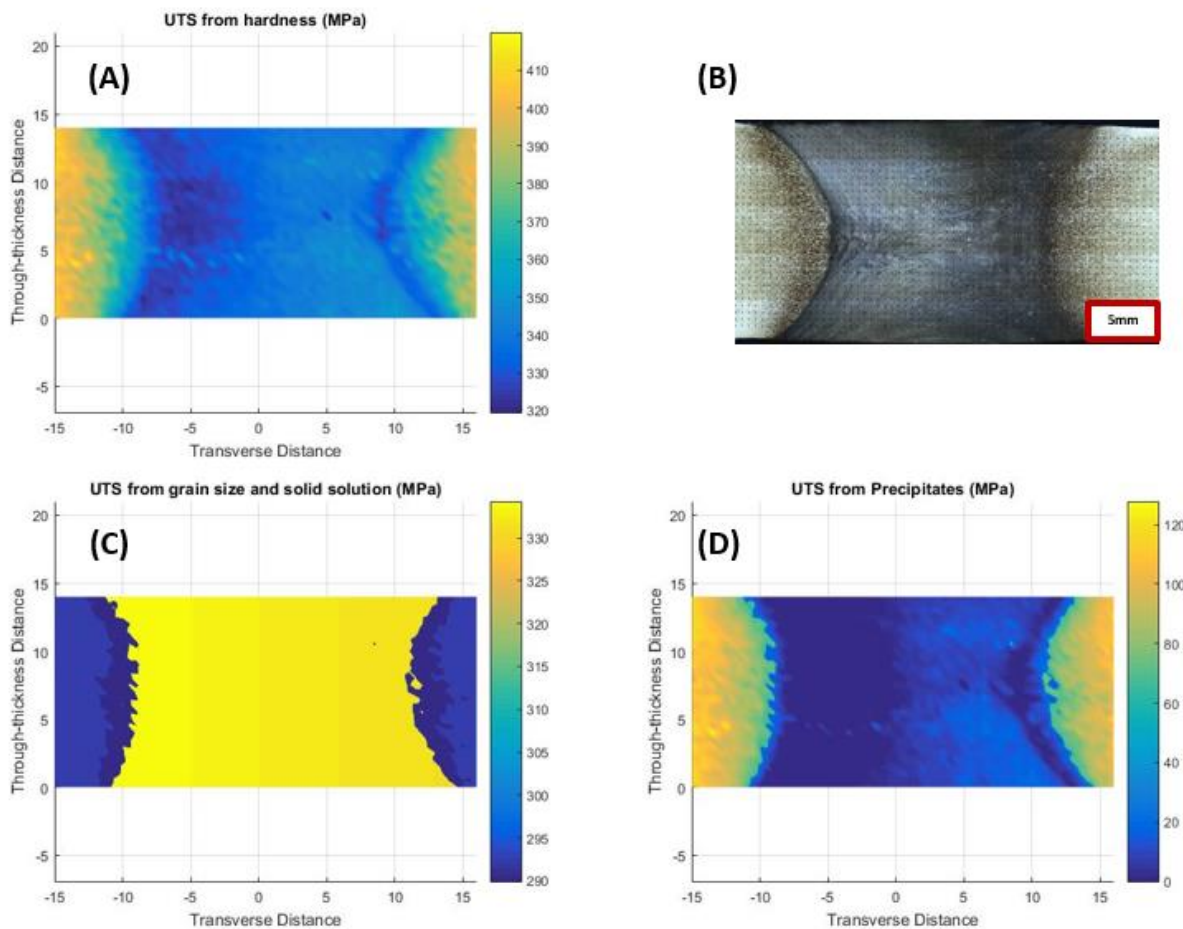


Figure A.13. Load-displacement plot for TMAZ  $K_{IC}$  sample.



*Figure A.14.* Model results of process parameter set #3. Low traversing speed, nominal tool rotational rate.



*Figure A.15.* Model results of process parameter set #4 High traversing speed, nominal tool rotational rate.